

Lawrence Berkeley National Laboratory

LBL Publications

Title

Cold-Season Precipitation Sensitivity to Microphysical Parameterizations:
Hydrologic Evaluations Leveraging Snow Lidar Datasets

Permalink

<https://escholarship.org/uc/item/2hf7n698>

Journal

Journal of Hydrometeorology, 25(1)

ISSN

1525-755X

Authors

Rudisill, WJ
Flores, AN
Marshall, HP
[et al.](#)

Publication Date

2024

DOI

10.1175/jhm-d-22-0217.1

Peer reviewed

1 **Cold-Season Precipitation Sensitivity to Microphysical Parameterizations:**
2 **Hydrologic Evaluations Leveraging Snow Lidar Datasets**

3 W.J. Rudisill,¹ A.N. Flores¹, H.P. Marshall¹, E. Siirila-Woodburn², D.R. Feldman², A.M.
4 Rhoades², Z. Xu², and A. Morales^{3,4}

5 ¹*Boise State University* ²*Earth and Environmental Sciences Area, Lawrence Berkeley National*
6 *Laboratory* ³*Cooperative Institute for Research in Environmental Sciences, University of*
7 *Colorado - Boulder* ⁴*NOAA Physical Sciences Laboratory*

8 *Corresponding author:* William Rudisill, williamrudisill@u.boisestate.edu

9 ABSTRACT: Cloud microphysical processes are an important facet of atmospheric modeling, as
10 they can control the initiation and rates of snowfall. Thus, parameterizations of these processes
11 have important implications for modeling seasonal snow accumulation. We conduct experiments
12 with the Weather Research and Forecasting (WRF V4.3.3) model using three different microphysics
13 parameterizations, including a sophisticated new scheme (ISHMAEL). Simulations are conducted
14 for two cold-seasons (2018 and 2019) centered on the Colorado Rockies' $\sim 750 \text{ km}^2$ East River
15 Watershed. Precipitation efficiencies are quantified using a drying-ratio mass budget approach
16 and point evaluations are performed against three NRCS SNOTEL stations. Precipitation and
17 meteorological outputs from each are used to force a land-surface model (Noah-MP) so that
18 peak snow accumulation can be compared against airborne snow lidar products. We find that
19 microphysical parameterization choice alone has a modest impact on total precipitation on the
20 order of $\pm 3\%$ watershed-wide, and as high as 15% for certain regions, similar to other studies
21 comparing the same parameterizations. Precipitation biases evaluated against SNOTEL are $15 \pm$
22 13% . WRF Noah-MP configurations produced snow water equivalents with good correlations with
23 airborne lidar products at a 1-km spatial resolution: Pearson's r values of 0.9, RMSEs between
24 8-17 cm and percent-biases of 3-15%. Noah-MP with precipitation from the PRISM geostatistical
25 precipitation product leads to a peak SWE underestimation of 32% in both years examined, and
26 a weaker spatial correlation than the WRF configurations. We fall short of identifying a clearly
27 superior microphysical parameterization, but conclude that snow lidar is a valuable non-traditional
28 indicator of model performance.

29 **1. Introduction**

30 Precipitation (rain and snowfall) in mountains is highly variable in space and time, under-
31 sampled by weather stations and radar, and challenging to model and measure (Lundquist et al.
32 2019). In mid-latitude regions, mountain precipitation often falls as snow, gradually accumulating
33 as snowpacks that act as natural reservoirs supporting ecosystems and human systems across the
34 watersheds into which they drain and beyond (Sturm et al. 2017; Siirila-Woodburn et al. 2021).
35 The streamflow from snowmelt depends not only on the antecedent snow-volume, but also spatial
36 location of snow accumulation throughout the watershed (Luce et al. 1998; Kiewiet et al. 2022).
37 The variability of snow accumulation occurs at a range of process scales spanning individual
38 hillslopes to synoptic scales (Clark et al. 2011). The value of seasonal snowpack in the Western
39 U.S. has been estimated in the trillions of dollars (Sturm et al. 2017), yet spatial estimates of the
40 water stored each winter remain poor in most areas. Snowfall is frequently the most uncertain
41 forcing variable in snow energy and mass balance models, and therefore remains a critical but
42 uncertain input for predicting this large natural reservoir (Raleigh et al. 2015).

43 A significant component of snowfall, and therefore where snowpacks accumulate, is caused
44 by orographic enhancement resulting from a variety of dynamical mechanisms including stable
45 upslope ascent from mechanical uplift, release of potential instabilities, lee-side convergence,
46 seeder-feeder processes, and convection triggered by differential heating associated with changes
47 in slope and aspect (Roe 2005; Houze 2012; Stoelinga et al. 2013; Kirshbaum et al. 2018).
48 Convection permitting atmospheric models (Prein et al. 2015) have demonstrated skill in modeling
49 precipitation accumulation in mountain environments where orographic enhancement processes
50 are important (Minder et al. 2008; Ikeda et al. 2010; Rasmussen et al. 2011; Gutmann et al. 2012;
51 He et al. 2019; Rudisill et al. 2021). For these reasons, and because of deficiencies in gridded
52 precipitation products (Henn et al. 2018), studies investigating the mountainous hydrologic cycle
53 and water resource management now frequently use output from numerical weather or climate
54 models (Lundquist et al. 2019; Meyer et al. 2023).

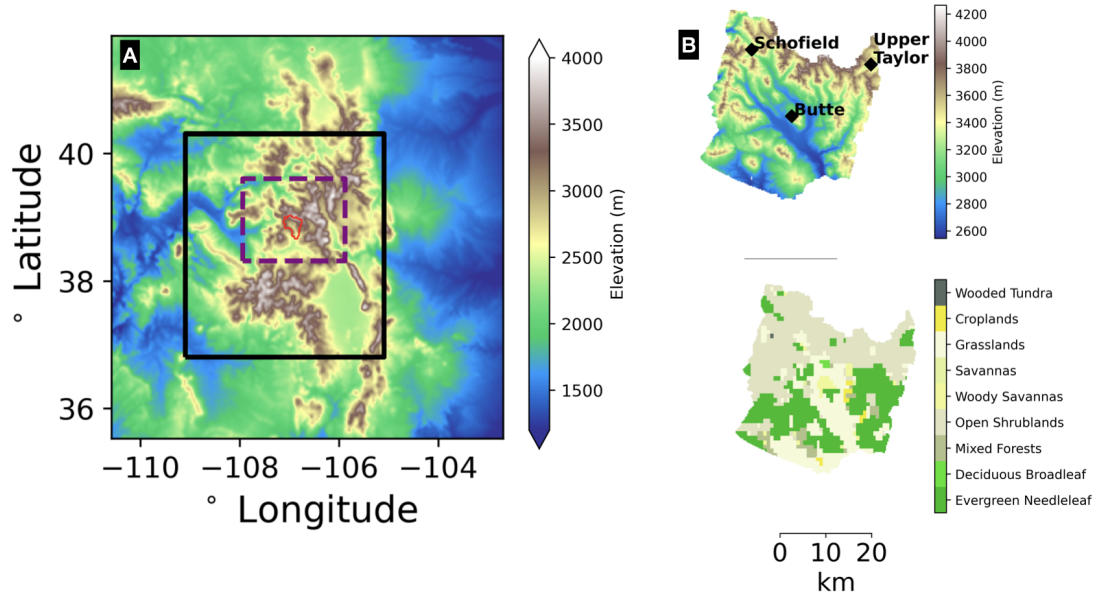
55 However, the predicted precipitation fields from atmospheric models exhibit errors from a wide
56 range of sources. For example, they are highly sensitive to the under-tested assumptions in mi-
57 crophysical parameterizations (Liu et al. 2011; Minder and Kingsmill 2013; Comin et al. 2018;
58 Rhoades et al. 2018; Rahimi et al. 2022). The problem is exacerbated in complex terrain where

59 the location of falling precipitation upwind/downwind of an orographic barrier can have important
60 hydrologic ramifications (Pavelsky et al. 2012). Unfortunately, the lack of comprehensive precip-
61 itation observations in complex terrain (Lundquist et al. 2019) creates an ill-posed process model
62 development and diagnostic premise: modeled precipitation is highly sensitive to model struc-
63 tural and parameterization choices, but those choices are not easily evaluated with observations.
64 This is because commonly used gridded precipitation datasets are highly uncertain in locations
65 far away from observations and can differ substantially in mountain regions (Henn et al. 2018).
66 Radar beams are frequently blocked in complex terrain limiting quantitative precipitation estimates
67 (Maddox et al. 2002). Consequently there is great need for better model evaluations in complex
68 mountain terrain.

69 At the same time, airborne Light Detection and Ranging (lidar) scanning is increasingly used
70 to monitor watershed scale montane snowpack, and provides high spatial resolution (1-5m-scale)
71 maps of snow depth (SD) and snow water equivalent (SWE) after making assumptions about
72 density (Painter et al. 2016). This is a trove of useful information, as the water content of a
73 seasonal snowpack tells us the lower-bound of the antecedent precipitation for that location. E.g.,
74 if the snowpack has one meter of water stored, and a model says that only 750 mm of precipitation
75 accumulated in that region, then we know the model is under predicting. Lidar SD is measured by
76 first mapping the snow-free land surface from aircraft. Subsequent flights during the snow season
77 record snow-top heights, which are differenced from the bare-ground elevation. The accuracy for
78 snow-height measurements in flat terrain is considered ± 8 cm for a 1 meter swath (Deems et al.
79 2013; Painter et al. 2016) in several studies, though some have reported values as high 20-30 cm for
80 certain vegetation types (Tinkham et al. 2014). Lidar SD can then be combined with model-derived
81 snow density estimates to produce spatial estimates of snow water equivalent (SWE). Densities can
82 be modeled using energy balance modeling (Hedrick et al. 2018), and generally vary less (spatially)
83 than SD (Sturm et al. 2010). Lidar flights represent only a single snapshot in time of the state of
84 the snowpack, and snow density estimates are limited by small observational datasets of density
85 in complex terrain. Still, when measured near the peak of the accumulation season, SWE can be a
86 very close measure of the antecedent snowfall received at that point, minus water lost to ablation,
87 and both positive and negative impacts of wind redistribution. Previous studies have leveraged
88 the strong relationship between precipitation processes and snow accumulation patterns to scale

89 precipitation forcings for use in hydrologic modeling (Vögeli et al. 2016; Pflug et al. 2021), to
90 examine precipitation-elevation gradients (Kirchner et al. 2014), and to evaluate the skill of various
91 precipitation datasets (Behrangi et al. 2018).

92 The goal of this study is several-fold. We seek to evaluate the sensitivities of simulated snowfall
93 in the Weather Research and Forecasting (WRF) model (Skamarock et al. 2019; Powers et al. 2017)
94 to three different microphysical parameterizations (or "schemes") of varying complexity across the
95 snow accumulation portions of two Water Years (WY; October through April of 2018 and 2019)
96 covering the vicinity of Colorado's East River Watershed (ERW) and surrounding regions (Figure
97 1) We evaluate the Morrison et al. (2005), Thompson et al. (2008), and recently developed Ice-
98 Spheroids Habit Model with Aspect-ratio EvoLution (ISHMAEL; Jensen et al. 2017) schemes. We
99 seek to 1) determine if the WRF model meteorology can produce snowpacks with similar spatial
100 patterns and magnitudes to what is observed by Airborne Snow Observatory (ASO; Painter et al.
101 2016) snow lidar, 2) identify which microphysical scheme is better, if any, as compared to ASO and
102 NRCS SNOTEL gauge data ("SNOW TELEmetry"; Serreze et al. 1999), and 3) examine if the WRF
103 model does better than the PRISM (Parameter Regression on Independent Slopes; Daly et al. 2008)
104 geostatistical precipitation product for matching the ASO snow product. The PRISM dataset is
105 commonly used for precipitation model validation in the Western US (e.g. Liu et al. 2017) so it is a
106 useful baseline to compare models against. Model point-scale biases of accumulated precipitation
107 are evaluated against three NRCS SNOTEL sites within the domain (Figure 1). To better understand
108 precipitation sensitivity to microphysics parameterizations, we also use a "drying ratio" method to
109 evaluate the efficiency of each model configuration for converting water vapor flux to precipitation,
110 based on Eidhammer et al. (2018). We also examine cross-section views of atmospheric quantities
111 across the ERW to better understand the differences between each WRF scheme. The ultimate
112 motivation of this study is to improve modeling capabilities of mountain cryosphere processes,
113 particularly in the water-resource essential Upper Colorado River basin where this study is located
114 (Tillman et al. 2022).



115 FIG. 1. A) WRF model inner (black box) and outer (map extent) domains with elevation shown. The East
 116 River Watershed (ERW) is outlined in red. The bounding box for drying-ratio calculations is also shown (purple
 117 dashed line). B) The Noah-MP static geographic data used for snow modeling. Topography from the ASO lidar
 118 digital elevation model (DEM; upper right) and USGS 24 category vegetation classification type (bottom right).
 119 Locations of NRCS SNOTEL locations (black diamonds) are also shown. The ASO domain extends slightly
 120 beyond the extent of the ERW.

121 2. Methods

122 a. Study Area

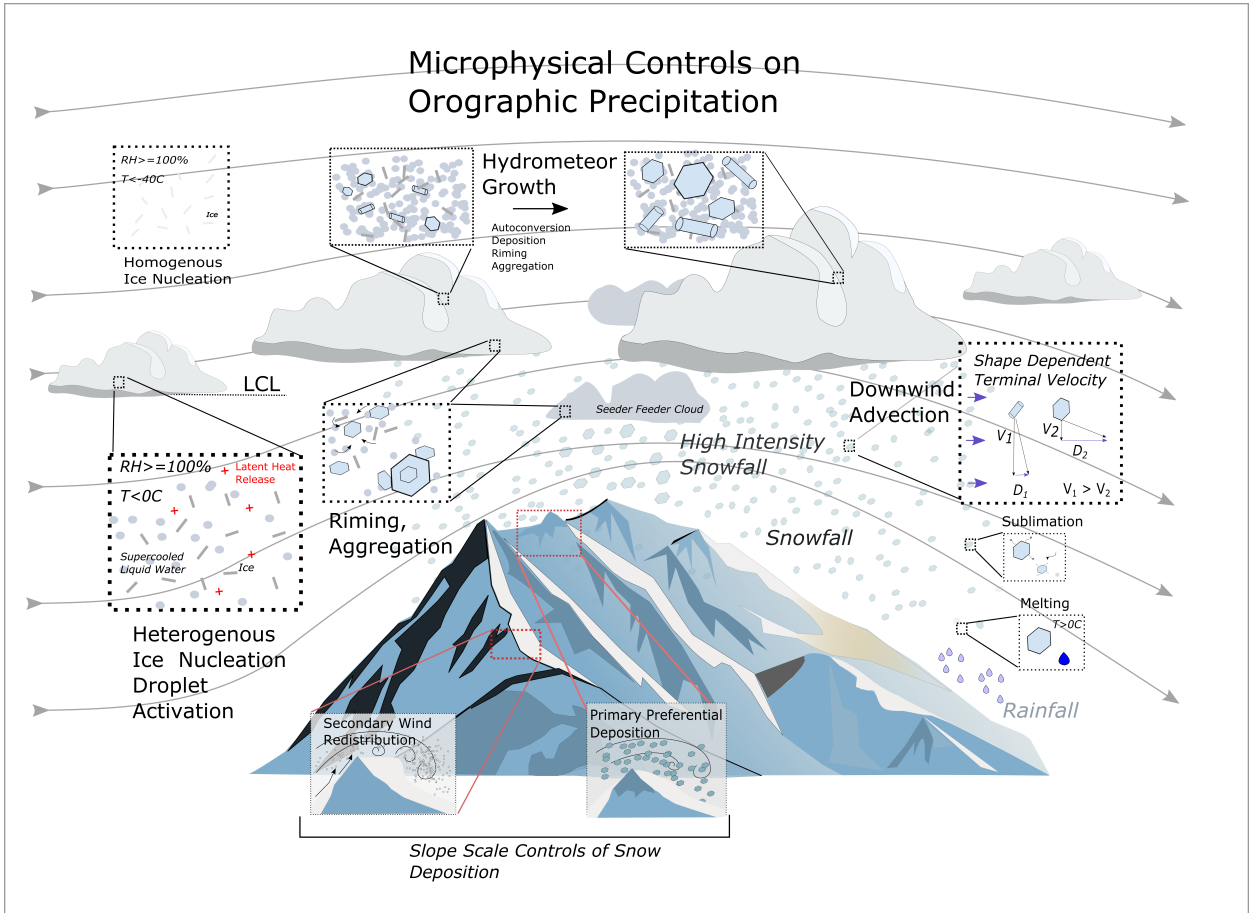
123 We focus our analysis on the ERW near Crested Butte, Colorado. The ERW is a high elevation
 124 (2500-3500 masl), representative Rocky Mountain watershed and the location of numerous critical
 125 zone, snow, and hydrologic studies (Hubbard et al. 2018), as well as a recently-deployed Department
 126 of Energy Atmospheric Radiation Measurement (ARM) field site (Feldman et al. 2021). The
 127 landcover types are predominantly open shrubland and evergreen needleleaf. The Airborne Snow
 128 Observatory (Painter et al. 2016) provides a lidar based SD and SWE product for WY2018-
 129 2019 covering the ERW with one flight near peak snow accumulation for WY2018 and 2019.
 130 Consequently, this watershed is an ideal testbed for examining microphysical, precipitation, and

131 snow processes, and model products will serve as guidance for hypothesis testing of ongoing field
132 observation campaigns. The study region technically extends beyond the ERW boundaries into the
133 Taylor and Castle creek watersheds, as ASO data covers these regions as well, and doing so allows
134 for comparisons against two additional NRCS SNOTEL monitoring sites.

135 *b. Microphysical Parameterizations*

136 It has been repeatedly shown that the representation of microphysical processes in atmospheric
137 models applied at regional to global scales can have a significant impact on modeled orographic
138 precipitation magnitude and spatial variability (Khain et al. 2000; Gettelman et al. 2019; Liu
139 et al. 2011; Rhoades et al. 2018). Fundamentally, the microphysical parameterization schemes
140 in atmospheric models attempt to represent removal of atmospheric water from a given model
141 grid-cell based on kinematic and thermodynamic conditions (Khain et al. 2000; Morrison et al.
142 2020). Schemes in operational models typically use “bulk” approaches, where the hydrometeor
143 mixing ratio (mass per mass of dry air), number concentrations (particles per unit volume), and
144 other hydrometeor properties are predicted for a limited number of species (graupel, rain, snow,
145 cloud-water, etc; Morrison et al. 2020). Figure 2 illustrates an idealized depiction of some of
146 the most prominent cloud microphysical processes that control distributions of precipitation in
147 mountain regions. Moist processes can also influence the dynamics through latent heat release
148 (Jiang 2003) and interactions with radiation (Chen et al. 2018).

153 In this study we test the Thompson (Thompson et al. 2008; hereafter MP08), Morrison (Morrison
154 et al. 2005; hereafter MP10) and ISHMAEL (Jensen et al. 2017; hereafter MP55) microphysical
155 schemes (Table 1). Each scheme treats ice phase hydrometeors and growth processes in different
156 ways. The MP10 and MP08 both use 5 separate hydrometeor categories: cloud liquid, cloud ice,
157 snow, graupel, and rain and predict mixing ratios for each. MP10 predicts the number concentration
158 for ice, rain, snow and graupel, whereas MP08 only predicts the number concentration for rain.
159 In MP10, all hydrometeors are assumed to be spherical, with mass-density relationships given
160 by $m(D) = \pi/6\rho_s D^3$. MP08 is similar but describes snowflakes as approximately planar, with
161 mass-diameter relationships given by $m(D) = 0.069D^2$. The most sophisticated scheme tested is
162 MP55 which forecasts higher-order moments of hydrometeor species beyond mixing ratios and
163 number concentrations at the expense of a higher computational cost. The MP55 scheme uses



149 FIG. 2. Conceptual diagram illustrating key microphysical process controls on orographic precipitation as a
 150 parcel moves across a mountain barrier. The lifting condensation level (LCL), temperature (T), relative humidity
 151 (RH), hydrometeor velocity (V), and advection distance (D) are depicted. Secondary controls on slope scale
 152 snow deposition/redeposition are also shown. Gray contours show hypothetical wind streamlines.

164 three ice categories in place of snow/graupel categories and models the evolution of snowflakes
 165 as oblate spheroids with two evolving axes a_i and c_i , such that the particle mass is given by
 166 $m(a, c) = \rho_i \frac{4}{3} \pi a_i^2 c_i$. Here, a_i is half the major axis for plate-like crystals and half the minor axis
 167 for column-like crystals, and c_i is half the minor axis for plate-like crystals and half the major axis
 168 for column-like crystals. Consequently, MP55 explicitly models both columnar and dendritic ice-
 169 habits (characterized by different a_i/c_i ratios), and the temperature dependent nucleation of each
 170 of these forms. It is important to note that the growth processes (e.g., collection, vapor deposition)

171 depend on the particle aspect ratio. Although we highlight some of the differences across the three
 172 microphysics schemes, there are a variety of other differences between the schemes, and a full
 173 accounting is beyond the scope of the present study.

Scheme	Abbreviation	Reference
Thompson	MP08	Thompson et al. (2008)
Morrison	MP10	Morrison et al. (2005)
ISHMAEL	MP55	Jensen et al. (2017)

TABLE 1. Weather Research and Forecasting (WRF) Model V4.3.3 Microphysics options examined in this study.

174 *c. Weather Research and Forecasting (WRF) Model Configuration*

175 This study tests precipitation from WRF atmospheric model version V4.3.3 and sensitivities to
 176 microphysical parameterizations therein (Skamarock et al. 2019; Powers et al. 2017). WRF solves
 177 the compressible, non-hydrostatic Euler equations using a third order Runge-Kutta timestepping
 178 method. Both simulations use a two-way nested domain. Table 2 lists WRF subgrid-scale
 179 parameterization schemes used in this study. Additional model configuration options including
 180 the entire WRF namelist are included in the supplementary material. Lateral boundary and initial
 181 conditions for the WRF simulations are provided by the Climate Forecast System Reanalysis
 182 Version 2 (CSFv2; Saha et al. 2014). CFSv2 has a 0.5° horizontal resolution (~ 55 km), and lateral
 183 boundary conditions are provided every 6 hours. Two nested domains are used, a ~ 3 km outer
 184 (230×349 grid cells) and a ~ 1 km inner grid (349×391 grid cells). A two-week spin-up period is
 185 used prior to the October 1 start date for each model run. The WRF meteorological outputs are then
 186 used to force a high-resolution (250 m dx/dy) offline configuration of the Noah-MP land surface
 187 model (Niu et al. 2011), providing peak SWE and SD that are comparable to the spatial resolutions
 188 provided by the ASO lidar-derived snow product (50 m).

189 In this study, the WRF model is run from October 1, 2017 - April 30, 2018 (part of WY2018)
 190 and October 1 2018 - April 30, 2019 (part of WY2019), respectively. These periods are chosen
 191 since they correspond with the typical snow-accumulation season for this watershed, and that the
 192 two ASO flight dates of interest are on March 31, 2018 and April 7, 2019 which are near the
 193 dates of peak SWE. In the paper we will refer to these time periods as WY2018 and WY2019

Physics Parameterization	Option	Reference
Convection	None	N/A
Microphysics	Thompson (MP08)	Thompson et al. (2008)
	Morrison (MP10)	Morrison et al. (2005)
	Ismael (MP55)	Jensen et al. (2017)
LSM	Noah-MP	Niu et al. (2011)
Surface Layer	Monin-Obukhov (Option 2)	Monin and Obukhov (1954)
Planetary Boundary Layer	Mellor-Yamada-Janjic (Eta/NMM) PBL	Janić (2001)
Longwave Radiation	Community Atmosphere Model (CAM)	Neale et al. (2010)
Shortwave Radiation	Community Atmosphere Model (CAM)	Neale et al. (2010)

TABLE 2. Weather Research and Forecasting (WRF) subgrid-scale physics parameterizations used in this study.

194 for convenience, even though they only represent the cold-season part of the year, not the entire
195 year. These years represent a fairly wet and a fairly dry cold-season, so fortunately we can test
196 the model for a range of snow conditions. Examining precipitation data from the NRCS Schofield
197 SNOTEL site shows that WY2019 is the 8th wettest (172.8 mm above average) and WY2018 the
198 23rd wettest (-68.5mm below average) out of 38 years of record. In addition, a fourth Noah-MP
199 experiment is conducted using precipitation from the PRISM dataset (Daly et al. 2008). PRISM
200 is a commonly used data product that is frequently used, either directly or indirectly, to generate
201 spatial precipitation forcings for model applications (Lundquist et al. 2019), so this experiment
202 serves as a useful benchmark test for the skill of WRF precipitation. PRISM is often used as a
203 benchmark dataset for atmospheric model development studies, so it is a good test for the baseline
204 of model performance.

205 *d. Model Performance Metrics*

206 The efficiency of each microphysical scheme is evaluated using the Drying Ratio (DR) method
207 (Eidhammer et al. 2018), which is in essence the accumulated precipitation normalized by the flux
208 of the integrated vapor transport. The components are given by:

$$F_{u,x} = -\frac{1}{g} * \int_{p_0}^{p_{Top}} \int_x \int_t q \mathbf{U} dP dx dt \quad (1)$$

$$F_{v,y} = -\frac{1}{g} * \int_{p_0}^{p_{Top}} \int_y \int_t q \nabla P dy dt \quad (2)$$

209 where p is atmospheric pressure, U and V are meridional/zonal winds, and q is the water vapor
 210 mixing ratio (kg/kg). The DR is then given by:

$$DR = \frac{P}{F} \quad (3)$$

211 where $F = F_{v,y} + F_{u,x}$ and P is mass of precipitation in kilograms. The DR calculation makes
 212 several assumptions, following Eidhammer et al. (2018). The assumptions are that non-vapor
 213 phases (clouds, ice, snow, etc.) are not included in the Q flux calculation (Equation 2), as the
 214 fraction of the total vapor is small. The contribution of local evaporation to local precipitation
 215 is also considered negligible. Year-to-year variation in precipitation accumulation could result
 216 from a fairly constant precipitation efficiency but moisture flux variability, precipitation efficiency
 217 variability alone, or a combination of both. The purpose of computing the drying ratio for the two
 218 study years is to help disentangle these factors. Eidhammer et al. (2018) used the DR to examine
 219 how the shapes of mountain ranges impact orographic precipitation for a single configuration of
 220 WRF. This study on the other hand examines one geographic region, but how the DR changes for
 221 different configurations of the WRF model. The DR is computed on a 145 by 180 grid cell box
 222 surrounding the ERW (Figure 1). The calculation is simplified as the direction of season average
 223 integrated vapor transport is uniformly from the southwest.

224 We apply several different metrics to evaluate model snowpack against ASO observations. Two
 225 primary quantities are assessed: the spatial locations of snow accumulation within the ERW, and
 226 the total watershed storage of snow at the evaluation time steps. The spatial locations of snow are
 227 important for modeling the temporal dynamics of snowmelt and runoff (Luce et al. 1998), while
 228 the total snow provides an estimate of the water contained in the snow reservoir.

229 To assess spatial pattern similarity, we use an objective function described in Demirel et al.
 230 (2017) and applied in a similar, recent snow modeling study (Wrzesien et al. 2022). This Spatial
 231 Efficiency (SPAEF) metric for two datasets x and y of length n are given by:

$$SPAEF = 1 - \sqrt{(1 - \gamma)^2 + (1 - \beta)^2 + (1 - r)^2} \quad (4)$$

232 where γ is the histogram intersection (Swain and Ballard (1991)), given by:

$$\gamma = \frac{\sum_{i=1}^n \min(K_i, J_i)}{\sum_{i=1}^n K_i} \quad (5)$$

233 where K and J are the respective histograms for datasets x and y . The histogram bin size is set
234 to 100. The β term in Equation 4 is given by:

$$\beta = \frac{\sigma_x}{\mu_x} \bigg/ \frac{\sigma_y}{\mu_y} \quad (6)$$

235 where σ and μ are standard deviations and means of x and y , and r is the Pearson correlation
236 coefficient (Pearson's r) and is given by:

$$r = \frac{\sum_{i=0}^n (x_i - \bar{x})(y_i - \bar{y})}{\sqrt{\sum_{i=0}^n (x_i - \bar{x})^2 \sum_{i=0}^n (y_i - \bar{y})^2}} \quad (7)$$

237 The histogram-intersection is performed after normalizing the data (subtracting the mean and
238 dividing by the standard deviation). Consequently, the SPAEF is designed to be a measure of spatial
239 similarity between two datasets x and y that is insensitive to biases in those datasets (Demirel et al.
240 2017). A perfect value of SPAEF (equivalent x and y) is 1.

241 In addition to the SPAEF and the Pearson's r , we evaluate the percent bias ($bias_p$), given by:

$$bias_p = \frac{(\sum_{i=1}^n x_i - \sum_{i=1}^n y_i)}{\sum_{i=1}^n y_i} * 100 \quad (8)$$

242 The percent bias is insensitive to the spatial agreement of each dataset and is determined to
243 measure watershed average snow quantity (depth or SWE) between the two datasets. Finally, we
244 compute the root mean square error (RMSE), given by

$$RMSE = \sqrt{\frac{1}{n} \sum_{i=0}^n (x_i - y_i)^2} \quad (9)$$

245 *e. Snowpack Modeling, ASO Data Processing, and SNOTEL Data Comparison*

246 Snowpack spatial variability, at the peak of the accumulation season, is shaped by a combination
247 of 1) precipitation variability, 2) slope scale preferential deposition, 3) secondary redistribution

248 (e.g., blowing snow), and 4) melt/sublimation (or loss) processes (Mott et al. 2018; illustrated in
249 Figure 2). Avalanches also redistribute snow on steep slopes typically greater than 30°. In order
250 to use ASO lidar snow data to evaluate precipitation variability, secondary redistribution and loss
251 processes must be taken into account. The following sections describe how ASO data is processed
252 for comparison purposes, and then how Noah-MP is configured to perform these tasks.

253 1) DATA PROCESSING

254 First, the ASO data in UTM spatial coordinates (downloaded from the NSIDC;
255 <https://nsidc.org/data/aso/data>) data are clipped to the region of interest. The data are bilinearly
256 resampled from 50 m to 250 m using the "gdalwarp" algorithm (<https://gdal.org/>). The gdalwarp
257 algorithm allows for several different resampling methods. Bi-linear is chosen, following other
258 studies that have similarly applied the same method to resample ASO snow products (Bair et al.
259 2016; Behrangi et al. 2018). The ASO data are then reprojected to a lat-lon coordinate system,
260 again using the gdalwarp method, and converted to netcdf file format. At this stage, to enable grid-
261 to-grid comparison, we use the xESMF python library (<https://xesmf.readthedocs.io/en/latest/>) and
262 again select a bi-linear interpolation method to align the ASO and Noah-MP model grids. We
263 compared the total SD between converted ASO data and the raw data, and found that there was a
264 very small difference overall. From there, we are able to compare the Noah-MP output grid cell to
265 grid cell against the ASO data product. We chose an analysis scale of 1 km, as this matches the
266 resolution of the parent WRF meteorology and wind-related features captured by ASO are likely
267 smoothed out. To illustrate the effects, Figure 3 shows the re-sampled SD data from 50 m to 1 km.
268 Wind redistribution is clearly present on the windward/leeward sides of ridges at 50 m, but at 1
269 km these high-frequency features are removed. This step is performed using the xarray "coarsen"
270 function.

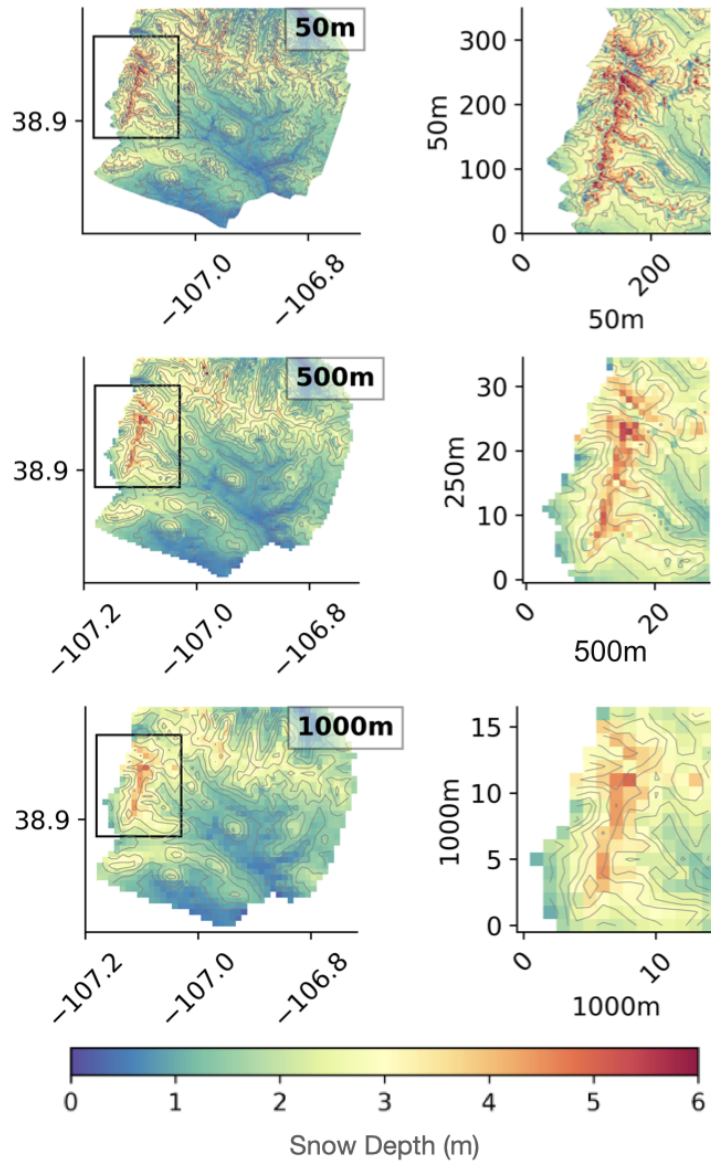
271 Converting SD to snow water equivalent requires estimates of snow density. While ASO produces
272 some density products using energy balance modeling, the snow densities distributed for 2018 and
273 2019 in the ERW were created using a linear regression between snow course observations of SD
274 and density (ASO Inc., personal communication). Consequently we chose to use the distributed,
275 spatially explicit snow densities produced by Noah-MP, averaged across the model runs produced
276 by this study to produce SWE estimates from the ASO depth products.

277 2) THE NOAH-MP MODEL

278 We use the Noah-MP model to account for snow ablation prior to the date of the ASO flight and to
279 model snow densities. Noah-MP can be used as a stand-alone land surface model, or can be coupled
280 with atmospheric models such as WRF. Niu et al. (2011) provides a technical description of the
281 model. We use the version of Noah-MP distributed with V5.1.1 of the WRF-Hydro (Gochis et al.
282 2018) modeling software, available online here: ([https://github.com/NCAR/wrf_hydro_](https://github.com/NCAR/wrf_hydro_nwm_public/releases/tag/v5.1.1)
283 [nwm_public/releases/tag/v5.1.1](https://github.com/NCAR/wrf_hydro_nwm_public/releases/tag/v5.1.1)). Noah-MP solves the energy and mass budgets of a multi-
284 layer snowpack taking into account sublimation, snowmelt, snow liquid-water retention, and canopy
285 interception among other processes. Noah-MP uses three snow layers. Noah-MP also uses a semi-
286 tile approach, such that there are separate flux calculations for the vegetated and non-vegetated
287 fraction of each grid cell. We use the same physics options that were implemented in the National
288 Water Model configuration of Noah-MP (as described in the technical documentation) as the
289 model was tested and vetted in a number of snow-dominated basins across the Western US.
290 Parameterizations relevant to this work include using the CLASS snow-albedo scheme (Verseghy
291 2007), the Jordan precipitation phase option (Jordan 1991), Monin-Obukov type surface layer
292 resistance for heat (option 1) Brutsaert (1982), and option 3 for canopy-radiation (Dickinson 1983;
293 Sellers 1985). The full Noah-MP namelist configuration is included in the supplementary material.

297 In addition to ASO data, we compare timeseries of WRF precipitation against accumulated
298 precipitation from three NRCS SNOTEL (Serreze et al. 1999) stations located in or near the ERW
299 (Figure 1). The Schofield, Butte, and Taylor are located to the North, in the Center, and to the East
300 of the ERW, respectively, and are each located approximately 20 km away from each other (Figure
301 1).

302 The ERW is a high elevation, continental watershed with cold temperatures, so we hypothesize
303 that both rain and melt prior to peak SWE are relatively minimal basin-wide. This hypothesis
304 is confirmed by analyzing SNOTEL data in the watershed, as the April 1 SWE (recorded at the
305 Butte SNOTEL snow pillow) is within $\pm 2\%$ of the accumulated precipitation (recorded at the
306 co-located precipitation gauge) on October 1 for the two years examined (Figure S1) and average
307 two-meter surface air temperatures are -4.5°C at the SNOTEL locations over the same time period.
308 Nevertheless, Noah-MP and the non-precipitation forcings are run and constructed for a 250 meter
309 regular latitude longitude grid based on the high-resolution DEM distributed with ASO. This is



294 FIG. 3. Airborne Snow Observatory (ASO) lidar derived SD for April 7, 2019 at three different resolutions (50
 295 m, 500 m, and 1 km) resampled using bi-linear interpolation. The black box in the left hand figures corresponds
 296 to the latitudinal and longitudinal extent of the figures on the right.

310 done because, while antecedent melt might be small basin-wide, forcing resolution and terrain
 311 related effects are important for snow simulations and there may be south facing locations with
 312 significant mid-winter ablation. Downscaling Noah-MP to 250 m is chosen, in part, based on results
 313 from Winstral et al. (2014) who examined the impact of various resolutions on snow simulation

314 accuracy, and found that 250 provided reasonable performance but was much degraded at coarser
315 scales.

316 First, the hourly WRF output variables are bi-linearly interpolated to the 250 meter grid. Then,
317 shortwave radiation, temperature, pressure, and specific humidity are adjusted to account for terrain
318 differences between the digital elevation model distributed with WRF and the higher-resolution
319 elevation model distributed by ASO. Temperature and pressure for each grid cell are adjusted via the
320 constant dry adiabatic lapse rate and hydrostatic relationship to match the updated digital elevation
321 model. Specific humidity is adjusted for elevation by assuming that the relative humidity (from
322 the original WRF data) is conserved, and specific humidity is adjusted to match the corrected air
323 temperature. The WRF downwelling shortwave radiation is converted to terrain-normal shortwave
324 radiation using terrain-geometry and solar angle relationships (Dingman 2015), using the slope
325 and aspect from the high resolution DEM. Terrain shadowing is not accounted for, but this impact
326 is assumed to be minimal at 1 km resolution. Longwave radiation and winds are not adjusted,
327 though corrections for terrain effects on shortwave and longwave radiation could improve the
328 simulations (Arthur et al. 2018; Feldman et al. 2022)) and could be pursued in future work. Some
329 studies have further downscaled wind-fields using empirical terrain relationships (Liston and Elder
330 2006) or physically-based solvers (Reynolds et al. 2021). Since Noah-MP does not simulate
331 wind redistribution, the benefits of more finely resolved wind fields are likely small (though wind
332 velocities do control rates of latent/sensible heat). The code to perform the forcing corrections is
333 available on GitHub (https://github.com/bsu-wrudisill/wrf_ERriv_mphys_aso).

334 **3. Results**

335 *a. Precipitation Accumulation Evaluation*

336 The timeseries of WRF modeled precipitation and two-meter surface air temperature from each
337 WRF microphysical scheme are compared against data from the three NRCS SNOTEL stations
338 (Figure 4). We don't show a comparison of PRISM against SNOTEL, since PRISM ingests
339 SNOTEL information, so this would not constitute an independent validation. The spatial scales
340 of orographic precipitation variability is apparent from looking at the SNOTEL data alone, as the
341 Schofield station receives almost twice the precipitation of the Butte site, and each site receives

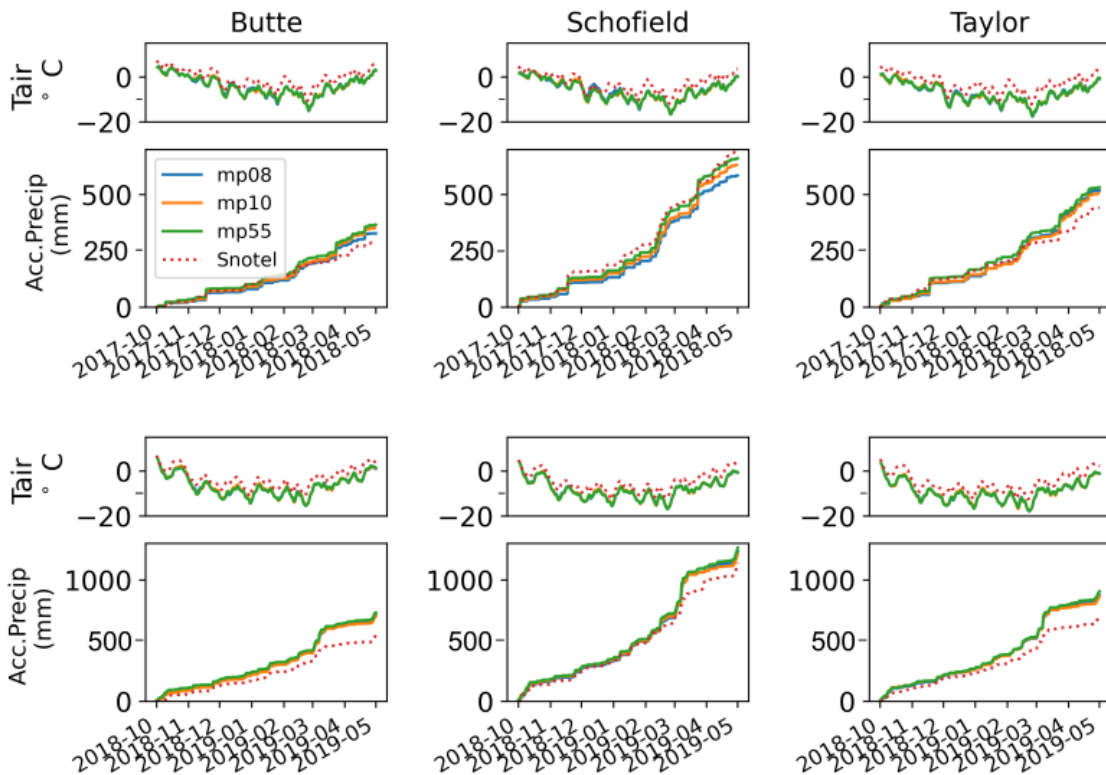
342 almost double the precipitation in 2019 compared to the previous year (~1200 mm versus ~650
343 mm at Schofield, for example).

344 MP55 consistently produces the most precipitation (across all sites and both years), and MP08
345 generally has the least precipitation (all but the Taylor in 2019; Figure 4). The WRF simulated
346 two-meter surface air temperatures are systematically cold biased by approximately 3°C across
347 microphysical schemes. Evaluated against the NRCS SNOTEL stations, WRF has a bias of 15
348 ±13% of accumulated precipitation at the end of the analysis period when averaged across each
349 all of the years and WRF schemes. Across the three sites, MP10 scheme performs the best for
350 both WY2018 (9.5% bias) and the WY2019 (16 % bias). These are just the biases from the three
351 grid-cells with SNOTEL observations. When the accumulated precipitation is averaged across the
352 entire ERW (not just at SNOTEL locations) the WRF configurations differ by slightly more than
353 2% of accumulated precipitation, but different regions within the watershed differ by as much as
354 10-15% (Figure S2).

358 The differences in precipitation accumulations can be expressed as the efficiency of dynamical/
359 microphysical processes for converting the incoming water vapor flux into precipitation. Figure
360 5 shows the DR averaged over October 1 to April 1 for each scheme and each WY. MP55
361 consistently has the highest DR, with almost double the DR values from WY2018 to WY2019.

364 *b. Vertical Atmospheric Profiles*

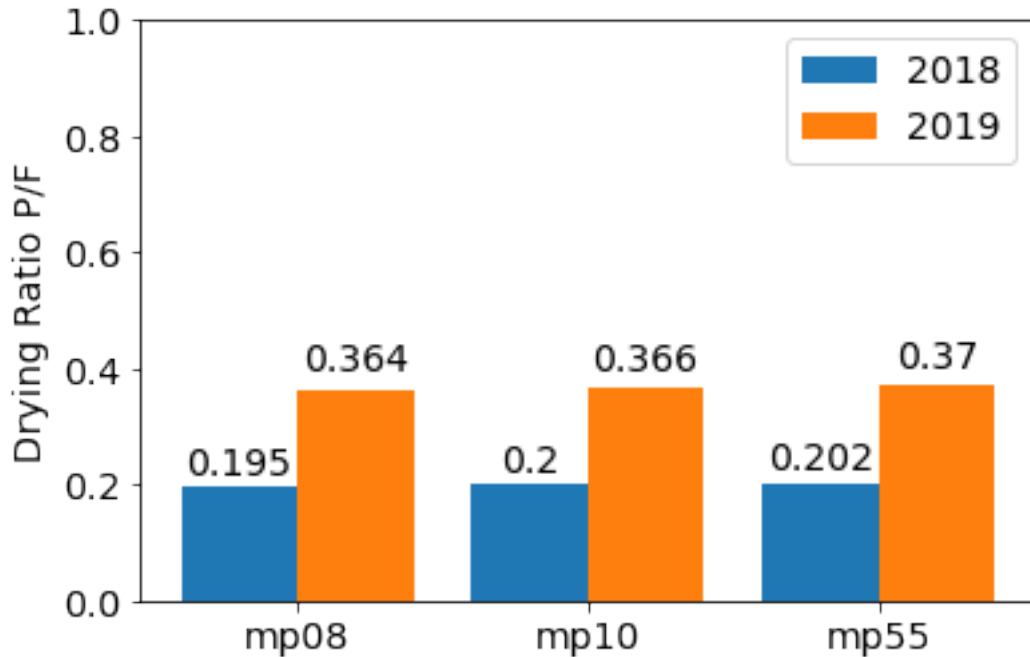
365 The temporally averaged (October 1 to April 1) cross section views of microphysical quantities,
366 cross-sectional winds (U and W components), and vertical velocities show the different locations
367 of ice-phase hydrometeor creation and fate, in addition to illuminating some of the precipitation
368 relevant dynamics (Figure 6). The ice-phases are lumped together snow and graupel for MP8 and
369 MP10, the three ice species in MP55. For all cases, the highest densities form a plume above of
370 the western watershed boundary, concentrated near the surface and decaying with height. MP55
371 has the highest densities across microphysical schemes, with a region of 3.0 g/kg during WY2018.
372 There is a consistent negative vertical velocity component on the lee-side of the western ridge
373 (Figure 6). Upstream of the ridge, there is a consistent low-level jet, characterized by a reversal
374 in the zonal wind direction (northerly, green dots) relative to the zonal wind (southerly) on the lee
375 side of the peak (not shown).



355 FIG. 4. Timeseries of WRF total accumulated precipitation (Acc. Precip, bottom) and two meter surface air
 356 temperature (Tair, top) compared against three NRCS SNOTEL sites, Butte, Schofield, and Taylor, for WY2018
 357 (first row) and WY2019 (second row).

381 *c. Modeled SWE and SD - Comparisons Against ASO Snow lidar*

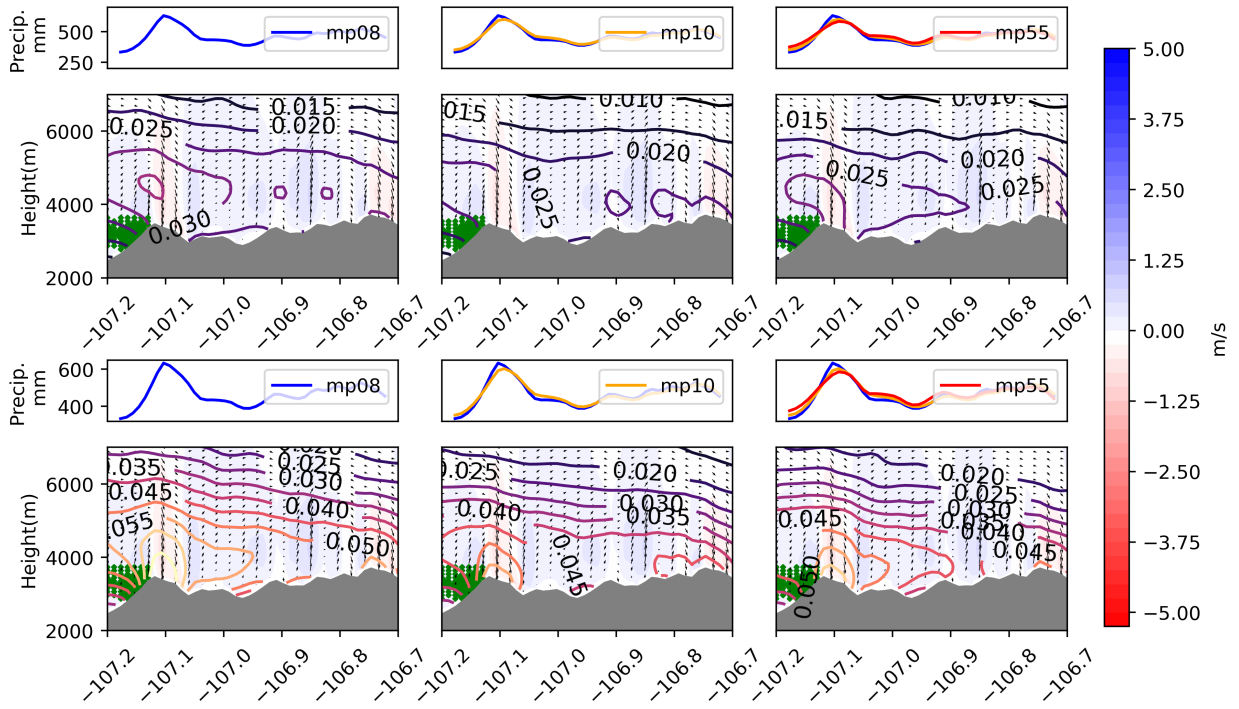
382 Figure 7 shows the results of comparing SD and SWE between ASO lidar products and each
 383 Noah-MP model forced with the three WRF model configurations (MP08, MP10, MP55) and a
 384 fourth test using the PRISM based precipitation data. Air temperature, radiation, winds, and all
 385 other non-precipitation meteorological forcings for the PRISM experiment come from the MP08
 386 WRF run. In order to compare SWE from model results to the ASO lidar product, an estimate of
 387 snow density is still required. We chose to use the average density from the Noah-MP model rather
 388 than the ASO densities.



362 FIG. 5. Drying Ratios (total precipitation normalized by incoming water vapor flux) computed for the greater
 363 ERW watershed region for October 1 to April 1 for WY2018 and WY2019, for each WRF microphysics scheme.

391 The fields from each model run are aggregated to a 1 km resolution from the native 250 m
 392 resolution for comparison of the final SWE values, and snow fields are plotted at the date of ASO
 393 acquisition (Figure 7). The RMSE computed at several analysis resolutions were examined from
 394 250 m to 8 km and we found the RMSE decreases asymptotically towards the mean-difference
 395 between the respective datasets (not shown). The northwest region of the watershed collects the
 396 most snow compared to the rest of the watershed, a pattern which is consistent for both years. The
 397 snow accumulation in ASO does not simply follow topography, as the western ridge delineating
 398 the watershed boundary is higher elevation than the northwestern ridge, which collects more snow.
 399 ASO has a more variable pattern of snow accumulation and higher maxima than any of the WRF-
 400 forced Noah-MP cases for both WY. The PRISM case has a smaller proportion of snow in the
 401 northwestern region compared to ASO and the WRF cases.

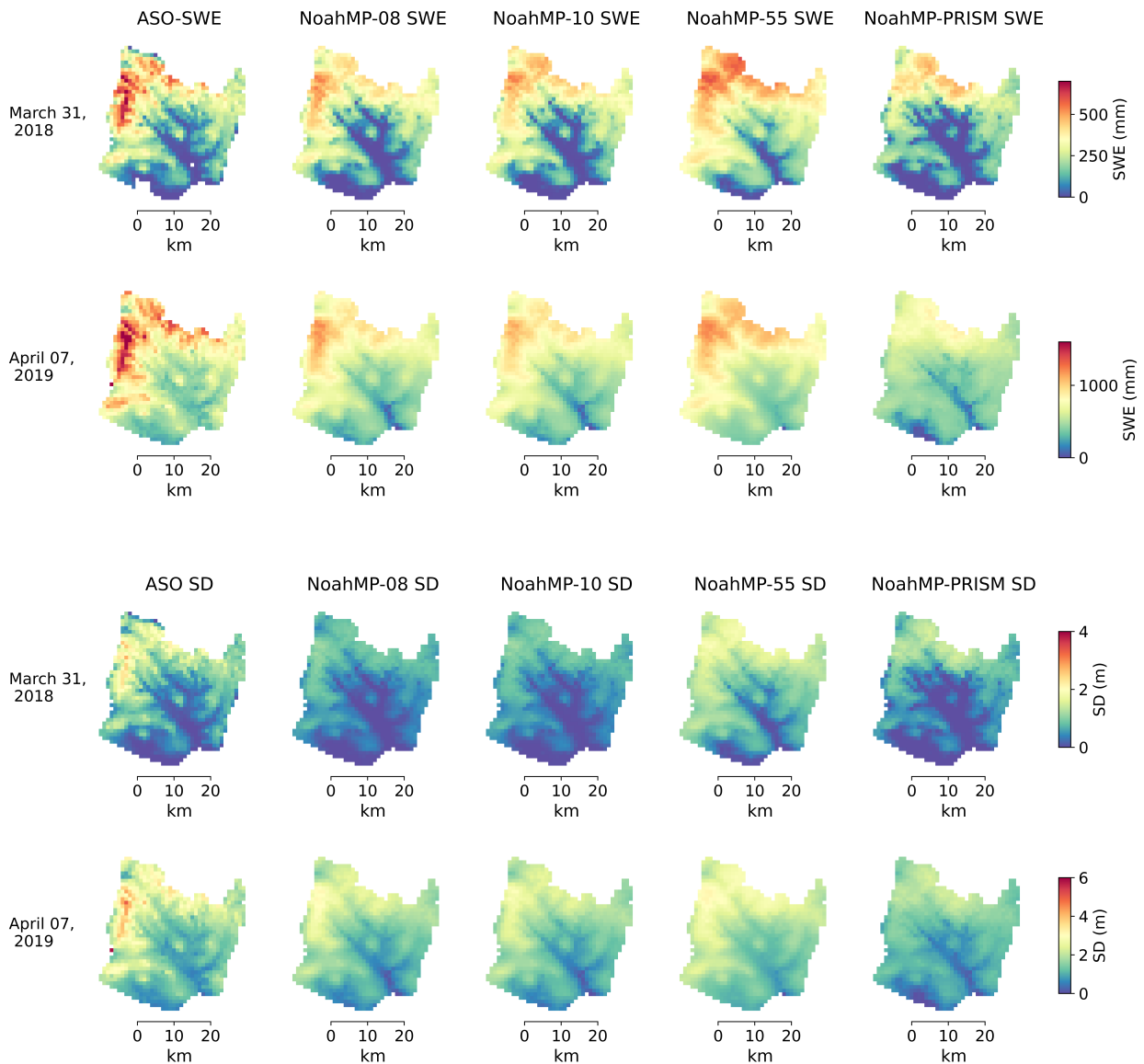
402 Table 3 shows summary statistics of the SWE and SD comparisons. The ASO data is treated as
 403 the reference for computing the bias. MP08 has the highest Pearson's correlation coefficient for
 404 both SWE and SD for both years, and the PRISM case has the worst correlations. Still all WRF-



376 FIG. 6. Cross sections of average directions of vertical windspeed (red/blue shading; units of m/s), vertical
 377 and zonal flow (arrows; units of m/s), and ice-phase hydrometeor concentrations (contours; units of g/kg dry
 378 air). Green dots show the regions where the average meridional wind speed reverses and is greater than 1 m/s).
 379 Accumulated precipitation (precip) along the transect is shown (top plots). WY2018 (2019) is shown in the top
 380 (bottom) row. The top of each plot shows cross sections of accumulated precipitation across the transect.

405 forced cases have a good spatial correlation with the ASO SWE ($r = .9$). The PRISM precipitation
 406 forced case has the lowest skill of all of the categories examined. The PRISM case underestimates
 407 watershed total snow accumulation ($\sim 32\text{-}36\%$) compared against the other WRF cases. The MP08
 408 simulated SWE has the lowest RMSE (8.45 cm) but MP55 has the lowest percent bias for 2018
 409 (12.0 %). MP55 has the lowest RMSE and percent bias for 2019 (13.6 cm; -2.5%).

412 The trend between elevation and snow accumulation illustrates some additional important dif-
 413 ferences between ASO and WRF (Figure 8). In each case, there is relatively little modeled melt
 414 except for the lower elevations (not shown). The average ASO SWE increase with elevation follows
 415 a linear pattern when a 200-grid cell rolling-mean window is applied, which approximately flattens
 416 out above approximately 3500 m. The SD (not shown) show the same leveling-off, so this is a
 417 function of a decrease in depths, not just an artifact of modeled densities. The slope of the SWE



389 FIG. 7. Comparison of WY2018 and WY2019 SWE (top two rows) and SD (bottom two rows) from ASO and
 390 Noah-MP. The labels (08, 10, 55, and PRISM) refer to the precipitation forcing used for Noah-MP.

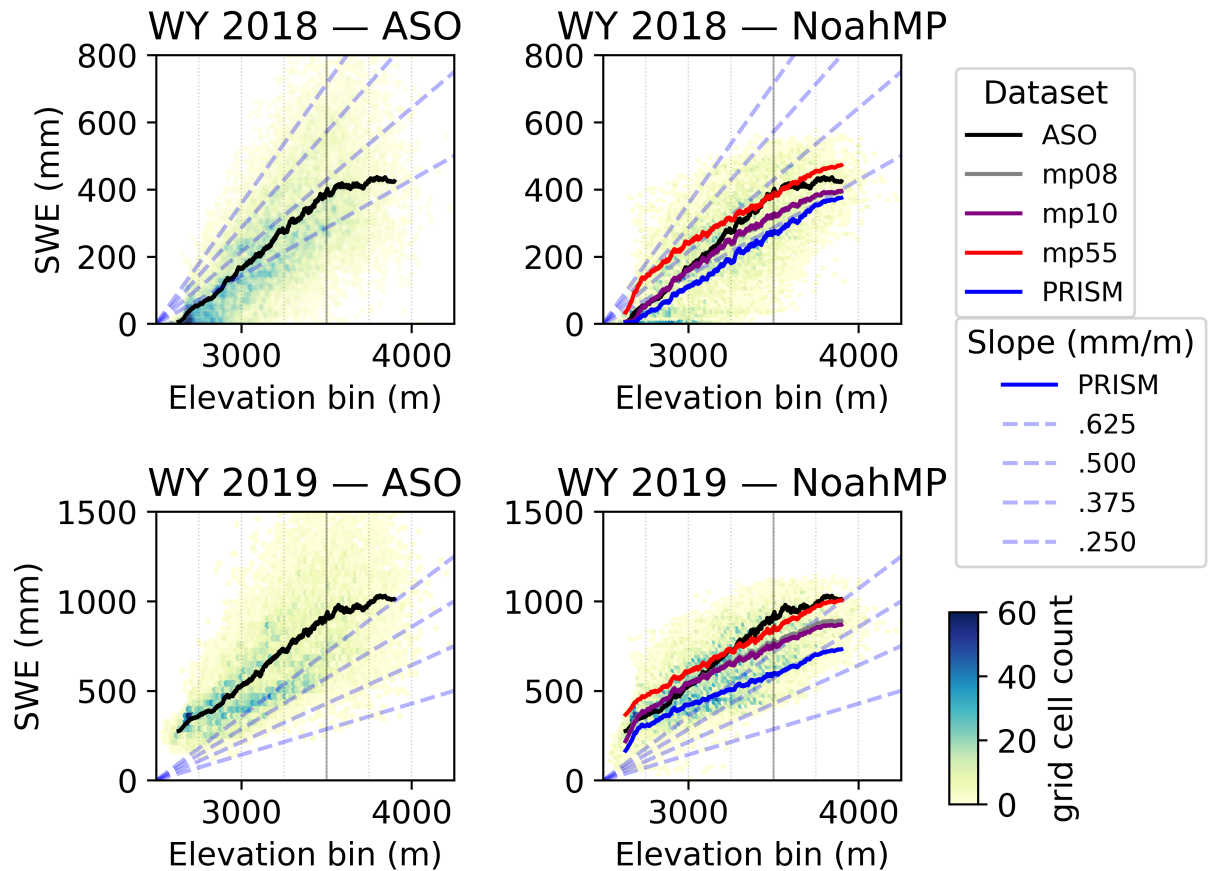
418 versus elevation line is higher for WY2019 and parallels the 0.625 mm of SWE per m of elevation,
 419 whereas 2018 more closely parallels the 0.50 mm/m line. The Noah-MP model SWE shows no
 420 such leveling out with elevation. The slopes of the Noah-MP curves are less-steep than the ASO
 421 data and shows the greatest spread during 2018. The variance of the ASO data increases with the
 422 magnitude (heteroskedasticity), which is not found in the WRF/Noah-MP modeled SWE.

Variable	Year	Model	Spatial		Mass Balance	
			r (unitless)	SPAEF (unitless)	RMSE (cm)	Bias (%)
Snow Water Equivalent (cm)	2018	Noah-MP-MP08	0.914	0.878	8.453	-15.498
		Noah-MP-MP10	0.905	0.870	8.603	-14.614
		Noah-MP-MP55	0.894	0.543	8.950	12.043
		Noah-MP-PRISM	0.821	0.805	13.133	-32.290
	2019	Noah-MP-MP08	0.922	0.832	15.947	-13.526
		Noah-MP-MP10	0.913	0.795	17.187	-14.713
		Noah-MP-MP55	0.908	0.688	13.600	-2.576
		Noah-MP-PRISM	0.785	0.706	30.605	-32.606
Snow Depth (cm)	2018	Noah-MP-MP08	0.913	0.902	26.798	-15.039
		Noah-MP-MP10	0.903	0.888	27.254	-13.823
		Noah-MP-MP55	0.896	0.539	30.026	19.270
		Noah-MP-PRISM	0.840	0.783	43.084	-36.093
	2019	Noah-MP-MP08	0.939	0.859	39.281	-12.851
		Noah-MP-MP10	0.924	0.800	43.496	-14.669
		Noah-MP-MP55	0.917	0.604	35.157	3.052
		Noah-MP-PRISM	0.811	0.780	77.039	-32.765

410 TABLE 3. Spatiotemporal and mass-balance error statistics for Noah-MP models compared against the ASO
411 lidar derived basin-wide SD and SWE estimates. Bold values denote the best performing scenario.

428 4. Discussion

429 This is the first study, to our knowledge, that has used airborne lidar derived snow products to
430 attempt to evaluate snowfall sensitivity to microphysical schemes in atmospheric models. To be



423 FIG. 8. SWE versus elevation relationships within the ERW. The left column shows density scatterplots of
 424 ASO derived SWE and the right column shows the same, but for the SWE from the Noah-MP simulations. The
 425 rolling-mean curves for the Noah-MP simulation and ASO product are shown. Lines with four different SWE
 426 versus elevation slopes (purple lines) are provided on each plot to better enable juxtaposition of datasets across
 427 different WY

431 clear, there are many other snow and atmospheric processes that must be understood to explain
 432 the elevation patterns of snow accumulation (Figure 8) including high-elevation snow deposition,
 433 redistribution, and sublimation processes. The issue of scale mismatches between models (such
 434 as WRF with a 1 km grid spacing) and observations (such as meter scale ASO lidar) presents a
 435 persistent challenge in snow-hydrology and hydrology in general (Blöschl 1999). Atmospheric
 436 water delivery processes operate across a wide range of scales, from cloud-particle to synoptic
 437 weather (see Figure 2), just as terrestrial processes influence snow variability. In this study, the
 438 decision was made to compute Noah-MP to ASO performance statistics at a 1 km resolution, rather

439 than the 250 m resolution of the Noah-MP model. This choice aimed to address unresolved features,
440 such as wind redistribution, which would likely contribute to model error (see Figure 3), while still
441 accounting for the impact of precipitation-induced variability. An natural question arises: Why not
442 run the model at 1 km resolution from the outset, without further downscaling of non-precipitation
443 forcings? (see Section 2) Initial testing revealed that model performance degraded compared to
444 the 250 m case, consistent with the findings of Winstral et al. (2014). Hence, the downscaling
445 approach proved valuable for isolating the dominant error sources. Nevertheless, understanding
446 the relationship between process scales, data resolution, and model evaluation scales remains a
447 crucial area of investigation. As argued by Blöschl (1999), optimal modeling element sizes are
448 influenced by data availability and the required resolutions of model predictions. Following this
449 philosophy, the model scale decisions in this study were carefully made.

450 Other studies have used snow lidar data to evaluate precipitation processes in various ways.
451 Kirchner et al. (2014) evaluated both PRISM (Daly et al. 2008) precipitation and statistical SWE
452 reconstructions against airborne lidar recorded near peak SWE accumulation in California. The
453 tapering-off of the SD/SWE with elevation relationship found in the ERW (Figure 8) was also
454 observed in that study. Behrangi et al. (2018) used ASO data to evaluate several precipitation
455 reconstructions in California's Tuolumne watershed. Our study found higher correlations between
456 WRF/Noah-MP and ASO than any of the datasets examined in that study, but worse RMSE and
457 biases (Behrangi et al. 2018; Table 3), which is also related to the scales of analysis (10 km versus
458 1 km). The RMSEs between Noah-MP SWE and ASO SWE are similar to other reports comparing
459 Noah-MP to ASO observations in Grand Mesa, Colorado (Wrzesien et al. 2022; Figure 12) at a
460 similar resolution. Wrzesien et al. (2022) also used a genetic calibration algorithm to calibrate
461 Noah-MP, a step which was not conducted here. Calibrating model parameters could possibly
462 reduce model structural errors, further isolating the errors caused by model forcings, however the
463 similarity of errors with Wrzesien et al. (2022) suggests that Noah-MP is reasonably configured
464 to model snow accumulation for this watershed and for the purposes of this study. Additionally,
465 we should note that all Noah-MP models had higher SWE and SD values at the lowest elevations
466 (less than 3000 m), which could be caused by a combination of underestimation in densification
467 processes, too much precipitation in valley bottoms, and/or not enough melt or sublimation loss
468 prior to the ASO lidar acquisition dates. Vegetation densities also change with elevation (Figure

469 1) which may influence the aforementioned snow processes through snow-canopy interactions.
470 Moreover, the heteroskedasticity of SWE/SD with elevation in the ASO products is another clear
471 feature not well-captured by Noah-MP. This could be due to avalanches or wind redistribution,
472 which are not modeled by Noah-MP. Better capturing the ASO observed elevation/precipitation
473 relationships in both atmospheric and snowpack models is a clear and testable objective for model
474 improvement identified in this study.

475 More tightly coupling the land surface model and microphysical schemes may improve the study
476 in a number of ways. The current version of Noah-MP does not accept solid/liquid precipitation
477 phases as input, and instead uses a partitioning scheme from Jordan (1991). Near surface air
478 temperature based methods do not always account for the range of microphysical processes, such
479 as cooling from latent heat release near the surface, that can lead to frozen phase precipitation
480 accumulations at a wider range of temperatures (Jennings et al. 2018). This might be a major
481 limitation in another watershed with lower elevations/warmer temperatures, but for each scheme
482 tested a small percentage of the precipitation fell as rain, regardless of partitioning method. Even
483 after bias correcting the two-meter surface air temperatures uniformly across the domain for
484 the -3°C bias compared against SNOTEL data (Figure 4) only the modeled SWE in the lowest
485 elevations of the watershed were significantly impacted. Consequently, performance of the different
486 microphysical schemes with respect to watersheds with larger rain-snow transition zones is untested
487 and could be an area of future research.

488 Another interesting product of this research is the large modeled DR for WY2019. Eidhammer
489 et al. (2018) reports lower DR more similar to that of WY2018, also for a region in Colorado,
490 but for individual storm events as opposed to an entire cold season. Some of the differences are
491 attributable to different WRF configurations and specific averaging regions used to compute the
492 DR. This investigation shows the increase in DR largely responsible for the higher precipitation
493 in 2019 compared to 2018, as opposed to an increase in water vapor flux, highlighting the role
494 of precipitation generating dynamic mechanisms. DR as high as 0.5 have been reported for the
495 Andes (Smith and Evans 2007) so the quantities reported in 2019 (a maximum of 0.37) are not
496 without precedent. The differences in DR between schemes could be a result of multiple factors.
497 Differences in the treatment of heterogeneous ice-nucleation (Morrison et al. 2020) are one possible

498 source of different computed DR. Additional work that examines specific microphysical tendencies
499 could isolate these specifics in greater detail, such as the analysis performed in Bao et al. (2019).

500 *a. Snowpack Density Uncertainties and Other Potential Improvements*

501 The largest uncertainty in estimating basin wide SWE from lidar derived snow-depth data comes
502 from estimating snow density (Raleigh and Small 2017). In this study, we used snow densities
503 simulated by Noah-MP to combine with ASO measured SD. In this way, the SWE and SD
504 comparisons (Figure 7) are not really independent. The density of new snow accumulation in the
505 Noah-MP follows Hedstrom and Pomeroy (1998) and depends on the two-meter air temperature
506 alone. Snowpack densification processes follow Anderson (1976) and Sun et al. (1999). ASO
507 also distributes a density product that is based on energy balance and/or empirical depth modeling
508 (ASO Inc., personal communication) but we chose to ignore it in this analysis. Incorporating
509 snow density observations is one avenue for improving this work. Better coupling between the
510 WRF microphysics scheme output and the snow model in Noah-MP could potentially improve
511 simulated snow densities. The bulk snowpack density depends on density of new snow, snow
512 metamorphosis, and compaction due to overburden (Colombo et al. 2019). Though untested in this
513 study, modifying the Jensen (MP55) or Thompson (MP08) schemes and the Noah-MP code so that
514 prognostic densities of snow and/or graupel are used by the land surface model, as opposed to re-
515 calculating snow densities in the land surface model, could potentially improve new snow density
516 estimates. The Morrison scheme (MP10) does not treat snow or graupel density as a prognostic
517 variable and the quantities are fixed at 100 and 500 kg/m^3 respectively, so better coupling MP10
518 would be of less utility. Moreover, coupling advanced schemes such as MP55 that explicitly model
519 hydrometeor shapes with snow process models may have additional utility for snow remote sensing
520 applications, where grain geometries complicate the retrieval of snow properties from radar signals
521 (Tsang et al. 2022).

522 Whether or not energetic forcings, such as shortwave and longwave radiation and sensible and
523 latent heat fluxes, that contribute to snow melt/densification are well represented is a significant
524 source of uncertainty in this study. Three dimensional longwave radiation effects from complex
525 terrain are not considered by WRF and can be significant (Feldman et al. 2021). With that said,
526 the observed cold-bias in WRF has been observed in other climate models (Rhoades et al. 2018,

527 2022) and may potentially be related to longwave radiation processes, too-stable boundary layers
528 over snow surfaces inhibiting heat exchanges (Slater et al. 2001), and/or other compensating biases
529 (e.g., cloud cover). However, sensitivity tests showed that correcting for biases had relatively little
530 effect on simulated peak SWE, particularly, for WY2019. Air temperatures at SNOTEL stations
531 have also been shown to have quality control and calibration issues (Oyler et al. 2015) that may or
532 may not be accounted for here, though comparisons with other meteorological station data near the
533 watershed (not shown) suggests this alone does not explain the biases. Therefore, we caution to the
534 hydrometeorological community that a more rigorous scrutiny of the temperature fields provided
535 by WRF simulations in complex, high elevation mountain terrain is needed. Comparing model
536 outputs with ASO lidar datasets during the ablation season was not performed for this study, but
537 could be another avenue to decompose simulated biases in temperature and radiation and identify
538 systemic structural issues in the models, as the condition of the ablation season snowpack will be
539 more sensitive to temperature and radiative forcings (in addition to other model parameterizations,
540 like snow albedo) that cause snowmelt.

541 *b. Comparison with other Microphysical Parameterization Sensitivity Studies*

542 Ultimately, the sensitivity of precipitation accumulation to microphysics choice is similar to
543 other studies that have compared the same options in WRF, but is much less than some that have
544 examined a wider range of options in the WRF model. Hughes et al. (2020) found that single
545 moment microphysics (WSM6) schemes were wetter than double-moment (Thompson/Morrison)
546 when evaluated over a single WY in the Sierra Nevada, and that precipitation accumulation was
547 more sensitive to microphysical parameterization choice than to lateral boundary conditions for
548 convection-permitting WRF simulations in the Sierra Nevada. Xu et al. (2022) tested the sensitivity
549 of WRF simulated meteorology to various subgrid parameterizations and boundary conditions for
550 a sub-region of the ERW. They found that a suite of physics options using the WSM6 scheme led
551 to 34% higher precipitation than simulations using the Thompson scheme, which is much higher
552 than the sensitivity found comparing MP08, MP10, and MP55 in this study. Liu et al. (2011)
553 examined a larger Colorado Rockies domain, and likewise found a modest ~2% difference between
554 the MP08 and MP10 schemes for a 3-month period across a Colorado Rockies subdomain (Table 2
555 of their paper), with spatial pattern differences that are somewhat similar, but across a much larger

556 area (Figure 6 of their paper). The PLIN scheme Chen and Sun (2002) however, also produced as
557 much as 30% higher precipitation than the Thompson scheme. Interestingly, the PLIN scheme also
558 showed a greater variance with elevation, which might better match reality in our study area (if
559 snowpack is a good proxy; Figure 8). Jensen et al. (2018) likewise compared MP08 and MP55 (in
560 addition to several others) for a case study in the Olympic Peninsula. They determine that MP55
561 responds less strongly to topography than MP10 and two additional scenarios where hydrometeor
562 growth in MP55 has been modified. Ultimately accumulated precipitation from MP55 differed
563 from MP10 by less than 4% during their 18-h study period (Table 2 of their study), though it is
564 unclear if that would change for longer evaluation period. Our simulation also produced very little
565 graupel from either MP08 or MP10 (Figure S3). Transitions from snow to graupel categories can
566 introduce artificially abrupt transitions in particle properties (such as density and fall speed) and
567 avoiding this is among the reasons that MP55 chooses to explicitly predict particle shapes rather
568 than a graupel category (Jensen et al. 2018), so a simulation where atmospheric conditions are
569 more favorable for graupel might show more spatial variability in precipitation. Ultimately, the
570 precipitation sensitivity to microphysics choice was fairly modest averaged across the watershed,
571 and in keeping with other studies that compared the same schemes. Testing other WRF options
572 (such as PLIN or WSM6) might reveal a greater variance in snowfall accumulation and performance
573 relative to ASO and SNOTEL.

574 Finally, while three schemes are tested in this study, each contains a range of parameters that
575 each have an uncertainty space that has been under-explored, such as assumed concentrations
576 of ice-nucleating particles. Idealized simulations show that perturbing individual parameters
577 within individual microphysics schemes can have a similar impact to using an entirely different
578 microphysics scheme (Morales et al. 2019). Future studies may consider producing an ensemble
579 of simulations that sample across a plausible range of these parameter values, informed by new
580 observational campaigns focused on mountain precipitation (Feldman et al. 2021).

581 **5. Conclusions**

582 High-altitude complex terrain is undergoing profound changes (Mountain Research Initiative
583 Edw Working Group et al. 2015) which are setting the stage for much-reduced snowpack in
584 the coming years and decades (Siirila-Woodburn et al. 2021). The details of the snowfall that

585 produces this snowpack are central to understanding the potential for changes in precipitation
586 amount and phase. Nowhere is this more apparent than in the Upper Colorado River Basin, which
587 is dramatically stressed due to both long-term warming trends (Milly and Dunne 2020) and recent
588 extreme drought (Williams et al. 2022). Since the East River Watershed (ERW) represents a
589 focused area of observations and research, collocated data and models of the ERW provide the
590 opportunity to develop new tests of uncertain model processes.

591 This study used a high resolution ASO lidar dataset of SD, collected near the peak of the
592 snow accumulation season in the ERW, to evaluate precipitation for three different microphysical
593 parameterizations (or schemes) implemented in the WRF model for both a high precipitation
594 (2019) and low precipitation (2018) cold-season (October through April) prior to the dates of
595 significant snowmelt. Model results show the magnitudes of precipitation between the years were
596 more controlled by precipitation efficiencies (higher/lower DR) compared to increases/decreases
597 in water vapor flux. All WRF configurations were able to capture the total precipitation evaluated
598 at three NRCS SNOTEL sites, with an average bias of $15\% \pm 13$ of accumulated precipitation at
599 the end of the analysis period. The MP55 scheme had a slightly higher DR and better matched both
600 SNOTEL and ASO observations for the high-snow volume year, but overpredicted precipitation
601 and snowpack for the dry-year (2018). Each microphysics scheme resulted in the development
602 of snowpacks with a high spatial correlation with ASO lidar datasets at a ~ 1 km scale, but the
603 Thompson (MP08) had the highest Pearson's correlation coefficient for both years examined. In
604 terms of bias and correlation, all WRF models produced snowpacks that better matched ASO data,
605 in particular in terms of bias, compared to the gauge-based statistical model estimates provided by
606 the PRISM precipitation product with the exception of one measure of spatial similarity (SPAEF).
607 Root mean square errors between the 1 km ASO lidar based SWE and WRF model products were
608 on the order of 8-13 cm (WY2018) and 13-15 cm (WY2019). Underestimations of cold-season
609 mountain precipitation from gridded products such as PRISM have been demonstrated in other
610 circumstances (Lundquist et al. 2015, 2019).

611 This study found ASO lidar snow datasets can potentially help evaluate microphysical scheme
612 fidelity, but more importantly high resolution regional climate models in poorly observed mountain
613 regions in general. Model deficiencies that may or may not be related to microphysical process are
614 also demonstrated, particularly with respect to snowpack/elevation patterns. While this study used

615 only two ASO lidar flights, other studies with longer data coverage have shown repeatability of
616 snow patterns to scale precipitation inputs into hydrologic models (Vögeli et al. 2016; Pflug et al.
617 2021). In the two ASO lidar flights used here, the locations of peak accumulation are consistently
618 on the northwestern ridge of the ERW on the windward side and the location of strongest uplift.
619 All models fail to create deep enough snowpacks in this region, highlighting a clear area of model
620 improvement, though it remains to be seen if improved microphysical parameterizations, finer grid
621 spacing, boundary conditions, or improvements to other model components are required to meet
622 this challenge. Revisiting the three questions posed in the introduction, we can conclude that 1)
623 WRF and Noah-MP does match ASO snowpack with good fidelity, but certain features are not well
624 captured (increasing snow depth variance with elevation; extreme accumulation on the NW ridge
625 of the watershed), 2) no single microphysics scheme emerges as clearly superior in terms of all of
626 the criteria examined, and 3) WRF does perform better at matching the ASO snow products than
627 the PRISM product.

628 The ability of any existing schemes to perform in out-of-sample conditions and additional
629 constraints must be demonstrated as well. There is a potential to do this using field campaigns
630 such as the Surface Atmosphere Integrated Field Laboratory (SAIL) for expanding upon the ASO
631 lidar data collection presented in this study. Such data can and should be used to further constrain
632 specific model microphysical process representations to establish if one or more schemes produce
633 consistent results relative to observations across more hydroclimatological states than we tested
634 here. We have demonstrated here that snowpack lidar products can be a useful diagnostic tool
635 for microphysics parameterizations across two WY, but the question of whether snowpack surveys
636 consistently constrain microphysics has not been demonstrated.

637 *Acknowledgments.* Rudisill was supported by the U.S. Department of Energy, Office of Science,
638 Office of Workforce Development for Teachers and Scientists, Office of Science Graduate Student
639 Research (SCGSR) program. The SCGSR program is administered by the Oak Ridge Institute for
640 Science and Education (ORISE) for the DOE. ORISE is managed by ORAU under contract number
641 DE-SC0014664. All opinions expressed in this paper are the authors' and do not necessarily reflect
642 the policies and views of DOE, ORAU, or ORISE. Rudisill and Flores acknowledge additional
643 funding from DOE BER grant DOE:DE-SC0019222. This research made use of Idaho National
644 Laboratory computing resources which are supported by the Office of Nuclear Energy of the
645 U.S. Department of Energy and the Nuclear Science User Facilities under Contract No. DE-AC07-
646 05ID14517. We also acknowledge high-performance computing support of the R2 compute cluster
647 (DOI: 10.18122/B2S41H) provided by Boise State University's Research Computing Department.
648 Rhoades was funded by the Director, Office of Science, Office of Biological and Environmental
649 Research of the U.S. Department of Energy Regional and Global Climate Modeling Program
650 (RGCM) "the Calibrated and Systematic Characterization, Attribution and Detection of Extremes
651 (CASCADE)" Science Focus Area (award no. DE-AC02-05CH11231) and the "An Integrated
652 Evaluation of the Simulated Hydroclimate System of the Continental US" project (award no. DE-
653 SC0016605). Feldman's material was based upon work supported by the U.S. Department of
654 Energy, Office of Science, Office of Biological and Environmental Research and the Atmospheric
655 System Research under U.S. Department of Energy Contract No. DE-AC02-05CH11231. Morales
656 was funded in part by the National Oceanic and Atmospheric Administration (NOAA) Cooperative
657 Agreement with the Cooperative Center for Environmental Sciences (CIRES), NA17OAR4320101.

658 *Data availability statement.* Model outputs from the Noah-MP snow model and forc-
659 ings are available on HydroShare (Rudisill, W. (2022). WRF-Mphys-ERiv, HydroShare,
660 <http://www.hydroshare.org/resource/8b3a213f2a26474cb2d473cbb4b0ca19>.
661 <https://thredds.hydroshare.org/thredds/catalog/hydroshare/resources/8b3a213f2a26474cb2d473cbb4b0ca19>
662 Airborne Snow Observatory data is publically available from the National Snow and
663 Ice data center <https://nsidc.org/data/aso/data>. PRISM precipitation data is available from
664 <https://prism.oregonstate.edu/>.

665 **References**

- 666 Anderson, E. A., 1976: A point of energy and mass balance model of a snow cover. *NOAA Tech.*
667 *Rep.*, **19**, 150.
- 668 Arthur, R. S., K. A. Lundquist, J. D. Mirocha, and F. K. Chow, 2018: Topographic effects on
669 radiation in the WRF model with the immersed boundary method: Implementation, validation,
670 and application to complex terrain. *Mon. Weather Rev.*, **146 (10)**, 3277–3292.
- 671 Bair, E. H., K. Rittger, R. E. Davis, T. H. Painter, and J. Dozier, 2016: Validating reconstruction
672 of snow water equivalent in California's Sierra Nevada using measurements from the NASA a
673 irborne Snow Observatory. *Water Resour. Res.*, **52 (11)**, 8437–8460.
- 674 Bao, J.-W., S. A. Michelson, and E. D. Grell, 2019: Microphysical process comparison of three
675 microphysics parameterization schemes in the WRF model for an idealized Squall-Line case
676 study. *Mon. Weather Rev.*, **147 (9)**, 3093–3120.
- 677 Behrangi, A., K. J. Bormann, and T. H. Painter, 2018: Using the airborne snow observatory to
678 assess remotely sensed snowfall products in the California Sierra Nevada. *Water Resour. Res.*,
679 **54 (10)**, 7331–7346.
- 680 Blöschl, G., 1999: Scaling issues in snow hydrology. *Hydrol. Process.*, **13 (14-15)**, 2149–2175.
- 681 Brutsaert, W., 1982: *Evaporation into the atmosphere*, 299pp., D. Reidel. Kluwer Academic Pub-
682 lishers.
- 683 Chen, C.-A., and Coauthors, 2018: Falling snow radiative effects enhance the global warming
684 response of the tropical Pacific atmosphere. *J. Geophys. Res.*, **123 (18)**, 10,109–10,124.
- 685 Chen, S.-H., and W.-Y. Sun, 2002: A one-dimensional time dependent cloud model. *J. Meteor.*
686 *Soc. Japan*, **80 (1)**, 99–118.
- 687 Clark, M. P., and Coauthors, 2011: Representing spatial variability of snow water equivalent in
688 hydrologic and land-surface models: A review. *Water Resour. Res.*, **47 (7)**.
- 689 Colombo, R., and Coauthors, 2019: Introducing thermal inertia for monitoring snowmelt processes
690 with remote sensing. *Geophys. Res. Lett.*, **46 (8)**, 4308–4319.

- 691 Comin, A. N., V. Schumacher, F. Justino, and A. Fernández, 2018: Impact of different microphys-
692 ical parameterizations on extreme snowfall events in the southern andes. *Weather and Climate*
693 *Extremes*, **21**, 65–75.
- 694 Daly, C., M. Halbleib, J. I. Smith, W. P. Gibson, M. K. Doggett, G. H. Taylor, J. Curtis, and
695 P. P. Pasteris, 2008: Physiographically sensitive mapping of climatological temperature and
696 precipitation across the conterminous united states. *Int. J. Climatol.*, **28** (15), 2031–2064.
- 697 Deems, J. S., T. H. Painter, and D. C. Finnegan, 2013: Lidar measurement of snow depth: a review.
698 *J. Glaciol.*, **59** (215), 467–479.
- 699 Demirel, M. C., J. Mai, G. Mendiguren, J. Koch, L. Samaniego, and S. Stisen, 2017: Combining
700 satellite data and appropriate objective functions for improved spatial pattern performance of a
701 distributed hydrologic model. *Hydrol. Earth Syst. Sci. Discuss.*, 1–22.
- 702 Dickinson, R. E., 1983: Land surface processes and climate—surface albedos and energy balance.
703 *Advances in geophysics*, Vol. 25, Elsevier, 305–353.
- 704 Dingman, L. S., 2015: *Physical Hydrology: Third Edition*. Waveland Press.
- 705 Eidhammer, T., V. Grubišić, R. Rasmussen, and K. Ikdea, 2018: Winter precipitation efficiency
706 of mountain ranges in the colorado rockies under climate change. *J. Geophys. Res.*, **123** (5),
707 2573–2590.
- 708 Feldman, D., and Coauthors, 2021: Surface atmosphere integrated field laboratory (sail) science
709 plan. Tech. rep., Oak Ridge National Lab.(ORNL), Oak Ridge, TN (United States), Atmospheric
710 Radiation Measurement (ARM) Data Center.
- 711 Feldman, D. R., M. Worden, N. Falco, P. J. Denny-Frank, J. Chen, B. Dafflon, and H. Wainwright,
712 2022: Three-dimensional surface downwelling longwave radiation clear-sky effects in the upper
713 colorado river basin. *Geophys. Res. Lett.*, **49** (4).
- 714 Gettelman, A., H. Morrison, K. Thayer-Calder, and C. M. Zarzycki, 2019: The impact of rimed
715 ice hydrometeors on global and regional climate. *J Adv Model Earth Syst*, **11** (6), 1543–1562.
- 716 Gochis, D., and Coauthors, 2018: WRF-Hydro model source code version 5. UCAR/NCAR.

717 Gutmann, E. D., R. M. Rasmussen, C. Liu, K. Ikeda, D. J. Gochis, M. P. Clark, J. Dudhia,
718 and G. Thompson, 2012: A comparison of statistical and dynamical downscaling of winter
719 precipitation over complex terrain. *J. Clim.*, **25** (1), 262–281.

720 He, C., F. Chen, M. Barlage, C. Liu, A. Newman, W. Tang, K. Ikeda, and R. Rasmussen, 2019:
721 Can convection-permitting modeling provide decent precipitation for offline high-resolution
722 snowpack simulations over mountains? *J. Geophys. Res.*, **124** (23), 12 631–12 654.

723 Hedrick, A. R., and Coauthors, 2018: Direct insertion of NASA airborne snow observatory-derived
724 snow depth time series into the isnobal energy balance snow model. *Water Resour. Res.*, **54** (10),
725 8045–8063.

726 Hedstrom, N. R., and J. W. Pomeroy, 1998: Measurements and modelling of snow interception in
727 the boreal forest. *Hydrol. Process.*

728 Henn, B., A. J. Newman, B. Livneh, C. Daly, and J. D. Lundquist, 2018: An assessment of
729 differences in gridded precipitation datasets in complex terrain. *J. Hydrol.*, **556**, 1205–1219.

730 Houze, R. A., Jr, 2012: Orographic effects on precipitating clouds. *Rev. Geophys.*, **50** (1).

731 Hubbard, S. S., and Coauthors, 2018: The east river, colorado, watershed: A mountainous commu-
732 nity testbed for improving predictive understanding of multiscale hydrological–biogeochemical
733 dynamics. *Vadose Zone J.*, **17** (1), 1–25.

734 Hughes, M., J. D. Lundquist, and B. Henn, 2020: Dynamical downscaling improves upon gridded
735 precipitation products in the sierra nevada, california. *Clim. Dyn.*, **55** (1), 111–129.

736 Ikeda, K., and Coauthors, 2010: Simulation of seasonal snowfall over colorado. *Atmos. Res.*, **97** (4),
737 462–477.

738 Janić, Z. I., 2001: Nonsingular implementation of the Mellor-Yamada level 2.5 scheme in the
739 NCEP meso model. Tech. rep., National Centers for Environmental Prediction Office.

740 Jennings, K. S., T. S. Winchell, B. Livneh, and N. P. Molotch, 2018: Spatial variation of the
741 rain-snow temperature threshold across the northern hemisphere. *Nat. Commun.*, **9** (1), 1148.

742 Jensen, A. A., J. Y. Harrington, and H. Morrison, 2018: Impacts of ice particle shape and density
743 evolution on the distribution of orographic precipitation. *J. Atmos. Sci.*, **75** (9), 3095–3114.

- 744 Jensen, A. A., J. Y. Harrington, H. Morrison, and J. A. Milbrandt, 2017: Predicting ice shape
745 evolution in a bulk microphysics model. *J. Atmos. Sci.*, **74** (6), 2081–2104.
- 746 Jiang, Q., 2003: Moist dynamics and orographic precipitation. *Tellus A*, **55** (4), 301–316.
- 747 Jordan, R. E., 1991: A one-dimensional temperature model for a snow cover : technical docu-
748 mentation for SNTHERM.89. Tech. rep., Cold Regions Research and Engineering Laboratory
749 (U.S.).
- 750 Khain, A., M. Ovtchinnikov, M. Pinsky, A. Pokrovsky, and H. Krugliak, 2000: Notes on the
751 state-of-the-art numerical modeling of cloud microphysics. *Atmos. Res.*, **55** (3), 159–224.
- 752 Kiewiet, L., E. Trujillo, A. Hedrick, S. Havens, K. Hale, M. Seyfried, S. Kampf, and S. E. Godsey,
753 2022: Effects of spatial and temporal variability in surface water inputs on streamflow generation
754 and cessation in the rain–snow transition zone. *Hydrol. Earth Syst. Sci.*, **26** (10), 2779–2796.
- 755 Kirchner, P. B., R. C. Bales, N. P. Molotch, J. Flanagan, and Q. Guo, 2014: LiDAR measurement of
756 seasonal snow accumulation along an elevation gradient in the southern sierra nevada, california.
757 *Hydrol. Earth Syst. Sci.*, **18** (10), 4261–4275.
- 758 Kirshbaum, D. J., B. Adler, N. Kalthoff, C. Barthlott, and S. Serafin, 2018: Moist orographic
759 convection: Physical mechanisms and links to Surface-Exchange processes. *Atmosphere*, **9** (3),
760 80.
- 761 Liston, G. E., and K. Elder, 2006: A meteorological distribution system for High-Resolution
762 terrestrial modeling (MicroMet). *J. Hydrometeorol.*, **7** (2), 217–234.
- 763 Liu, C., K. Ikeda, G. Thompson, R. Rasmussen, and J. Dudhia, 2011: High-Resolution simu-
764 lations of wintertime precipitation in the colorado headwaters region: Sensitivity to physics
765 parameterizations. *Mon. Weather Rev.*, **139** (11), 3533–3553.
- 766 Liu, C., and Coauthors, 2017: Continental-scale convection-permitting modeling of the current
767 and future climate of north america. *Clim. Dyn.*, **49** (1), 71–95.
- 768 Luce, C. H., D. G. Tarboton, and K. R. Cooley, 1998: The influence of the spatial distribution of
769 snow on basin-averaged snowmelt. *Hydrol. Process.*, **12** (10-11), 1671–1683.

- 770 Lundquist, J., M. Hughes, E. Gutmann, and S. Kapnick, 2019: Our skill in modeling mountain
771 rain and snow is bypassing the skill of our observational networks. *Bull. Am. Meteorol. Soc.*,
772 **100 (12)**, 2473–2490.
- 773 Lundquist, J. D., M. Hughes, B. Henn, E. D. Gutmann, B. Livneh, J. Dozier, and P. Neiman,
774 2015: High-Elevation precipitation patterns: Using snow measurements to assess daily gridded
775 datasets across the sierra nevada, california. *J. Hydrometeorol.*, **16 (4)**, 1773–1792.
- 776 Maddox, R. A., J. Zhang, J. J. Gourley, and K. W. Howard, 2002: Weather radar coverage over the
777 contiguous united states. *Weather Forecast.*, **17 (4)**, 927–934.
- 778 Meyer, J., J. Horel, P. Kormos, A. Hedrick, E. Trujillo, and S. M. Skiles, 2023: Operational
779 water forecast ability of the HRRR-iSnoBal combination: an evaluation to adapt into production
780 environments. *Geoscientific Model Development*, **16 (1)**, 233–250.
- 781 Milly, P. C. D., and K. A. Dunne, 2020: Colorado river flow dwindles as warming-driven loss of
782 reflective snow energizes evaporation. *Science*, **367 (6483)**, 1252–1255.
- 783 Minder, J. R., D. R. Durran, G. H. Roe, and A. M. Anders, 2008: The climatology of small-scale
784 orographic precipitation over the olympic mountains: Patterns and processes. *Quart. J. Roy.
785 Meteor. Soc.*, **134 (633)**, 817–839.
- 786 Minder, J. R., and D. E. Kingsmill, 2013: Mesoscale variations of the atmospheric snow line over
787 the northern sierra nevada: Multiyear statistics, case study, and mechanisms. *J. Atmos. Sci.*,
788 **70 (3)**, 916–938.
- 789 Monin, A. S., and A. M. Obukhov, 1954: Osnovnye zakonomernosti turbulentnogo peremeshivaniya
790 v prizemnom sloe atmosfery (basic laws of turbulent mixing in the atmosphere near the ground).
791 *Trudy geofiz. inst. AN SSSR*, **24 (151)**, 163–187.
- 792 Morales, A., D. J. Posselt, H. Morrison, and F. He, 2019: Assessing the influence of microphysical
793 and environmental parameter perturbations on orographic precipitation. *J. Atmos. Sci.*, **76 (5)**,
794 1373–1395.
- 795 Morrison, H., J. A. Curry, and V. I. Khvorostyanov, 2005: A new Double-Moment microphysics
796 parameterization for application in cloud and climate models. part i: Description. *J. Atmos. Sci.*,
797 **62 (6)**, 1665–1677.

- 798 Morrison, H., and Coauthors, 2020: Confronting the challenge of modeling cloud and precipitation
799 microphysics. *J Adv Model Earth Syst*, **12** (8), e2019MS001 689.
- 800 Mott, R., V. Vionnet, and T. Grünwald, 2018: The seasonal snow cover dynamics: Review on
801 Wind-Driven coupling processes. *Front Earth Sci. Chin.*, **6**.
- 802 Mountain Research Initiative Edw Working Group, and Coauthors, 2015: Elevation-dependent
803 warming in mountain regions of the world. *Nat. Clim. Chang.*, **5**, 424–430.
- 804 Neale, R. B., and Coauthors, 2010: Description of the NCAR community atmosphere model (CAM
805 5.0). *NCAR Tech. Note NCAR/TN-486+ STR*, **1** (1), 1–12.
- 806 Niu, G.-Y., and Coauthors, 2011: The community noah land surface model with multiparameteri-
807 zation options (Noah-MP): 1. model description and evaluation with local-scale measurements.
808 *J. Geophys. Res.*, **116** (D12).
- 809 Oyler, J. W., S. Z. Dobrowski, A. P. Ballantyne, A. E. Klene, and S. W. Running, 2015: Artificial
810 amplification of warming trends across the mountains of the western united states. *Geophys.*
811 *Res. Lett.*, **42** (1), 153–161.
- 812 Painter, T. H., and Coauthors, 2016: The airborne snow observatory: Fusion of scanning lidar,
813 imaging spectrometer, and physically-based modeling for mapping snow water equivalent and
814 snow albedo. *Remote Sens. Environ.*, **184**, 139–152.
- 815 Pavelsky, T. M., S. Sobolowski, S. B. Kapnick, and J. B. Barnes, 2012: Changes in orographic
816 precipitation patterns caused by a shift from snow to rain. *Geophys. Res. Lett.*, **39** (18).
- 817 Pflug, J. M., M. Hughes, and J. D. Lundquist, 2021: Downscaling snow deposition using historic
818 snow depth patterns: Diagnosing limitations from snowfall biases, winter snow losses, and
819 interannual snow pattern repeatability. *Water Resour. Res.*, **57** (8).
- 820 Powers, J. G., and Coauthors, 2017: The weather research and forecasting model: Overview,
821 system efforts, and future directions. *Bull. Am. Meteorol. Soc.*, **98** (8), 1717–1737.
- 822 Prein, A. F., and Coauthors, 2015: A review on regional convection-permitting climate modeling:
823 Demonstrations, prospects, and challenges. *Rev. Geophys.*, **53** (2), 323–361.

- 824 Rahimi, S., W. Krantz, Y.-H. Lin, B. Bass, N. Goldenson, A. Hall, Z. J. Lebo, and J. Norris, 2022:
825 Evaluation of a reanalysis-driven configuration of WRF4 over the western united states from
826 1980 to 2020. *J. Geophys. Res.*, **127** (4).
- 827 Raleigh, M. S., J. D. Lundquist, and M. P. Clark, 2015: Exploring the impact of forcing error char-
828 acteristics on physically based snow simulations within a global sensitivity analysis framework.
829 *Hydrol. Earth Syst. Sci.*, **19** (7), 3153–3179.
- 830 Raleigh, M. S., and E. E. Small, 2017: Snowpack density modeling is the primary source of
831 uncertainty when mapping basin-wide SWE with lidar. *Geophys. Res. Lett.*, **44** (8), 3700–3709.
- 832 Rasmussen, R., and Coauthors, 2011: High-Resolution coupled climate runoff simulations of
833 seasonal snowfall over colorado: A process study of current and warmer climate. *J. Clim.*,
834 **24** (12), 3015–3048.
- 835 Reynolds, D. S., J. M. Pflug, and J. D. Lundquist, 2021: Evaluating wind fields for use in basin-scale
836 distributed snow models. *Water Resour. Res.*, **57** (2).
- 837 Rhoades, A., and Coauthors, 2022: Asymmetric emergence of low-to-no snow in the midlatitudes
838 of the american cordillera, <https://doi.org/10.1038/s41558-022-01518-y>, .
- 839 Rhoades, A. M., P. A. Ullrich, C. M. Zarzycki, H. Johansen, S. A. Margulis, H. Morrison, Z. Xu, and
840 W. D. Collins, 2018: Sensitivity of mountain hydroclimate simulations in variable-resolution
841 CESM to microphysics and horizontal resolution. *J. Adv. Model. Earth Syst.*, **10** (6), 1357–1380.
- 842 Roe, G. H., 2005: Orographic precipitation. *Annu. Rev. Earth Planet. Sci.*, **33** (1), 645–671.
- 843 Rudisill, W., A. Flores, and J. McNamara, 2021: The impact of initial snow conditions on the
844 numerical weather simulation of a northern rockies atmospheric river. *J. Hydrometeorol.*, **22** (1),
845 155–167.
- 846 Saha, S., and Coauthors, 2014: The NCEP climate forecast system version 2. *J. Clim.*, **27** (6),
847 2185–2208.
- 848 Sellers, P. J., 1985: Canopy reflectance, photosynthesis and transpiration. *International journal of*
849 *remote sensing*, **6** (8), 1335–1372.

850 Serreze, M. C., M. P. Clark, R. L. Armstrong, D. A. McGinnis, and R. S. Pulwarty, 1999:
851 Characteristics of the western united states snowpack from snowpack telemetry (SNOTEL)
852 data. *Water Resour. Res.*, **35** (7), 2145–2160.

853 Siirila-Woodburn, E. R., and Coauthors, 2021: A low-to-no snow future and its impacts on water
854 resources in the western united states. *Nature Reviews Earth & Environment*, **2** (11), 800–819.

855 Skamarock, W. C., and Coauthors, 2019: A description of the advanced research WRF model
856 version 4. *National Center for Atmospheric Research: Boulder, CO, USA*, 145.

857 Slater, A. G., and Coauthors, 2001: The representation of snow in land surface schemes: Results
858 from PILPS 2(d). *J. Hydrometeorol.*, **2** (1), 7–25.

859 Smith, R. B., and J. P. Evans, 2007: Orographic precipitation and water vapor fractionation over
860 the southern andes. *J. Hydrometeorol.*, **8** (1), 3–19.

861 Stoelinga, M. T., R. E. Stewart, G. Thompson, and J. M. Thériault, 2013: Microphysical processes
862 within winter orographic cloud and precipitation systems. *Mountain Weather Research and*
863 *Forecasting: Recent Progress and Current Challenges*, F. K. Chow, S. F. J. De Wekker, and B. J.
864 Snyder, Eds., Springer Netherlands, Dordrecht, 345–408.

865 Sturm, M., M. A. Goldstein, and C. Parr, 2017: Water and life from snow: A trillion dollar science
866 question. *Water Resour. Res.*

867 Sturm, M., B. Taras, G. E. Liston, C. Derksen, T. Jonas, and J. Lea, 2010: Estimating snow water
868 equivalent using snow depth data and climate classes. *J. Hydrometeorol.*, **11** (6), 1380–1394.

869 Sun, S., J. Jin, and Y. Xue, 1999: A simple snow-atmosphere-soil transfer model. *J. Geophys. Res.*,
870 **104** (D16), 19 587–19 597.

871 Swain, M. J., and D. H. Ballard, 1991: Color indexing. *Int. J. Comput. Vis.*, **7** (1), 11–32.

872 Thompson, G., P. R. Field, R. M. Rasmussen, and W. D. Hall, 2008: Explicit forecasts of winter
873 precipitation using an improved bulk microphysics scheme. part ii: Implementation of a new
874 snow parameterization. *Monthly Weather Review*, **136** (12), 5095–5115.

875 Tillman, F. D., N. K. Day, M. P. Miller, O. L. Miller, C. A. Rumsey, D. R. Wise, P. C. Longley,
876 and M. C. McDonnell, 2022: A review of current capabilities and science gaps in water supply

877 data, modeling, and trends for water availability assessments in the upper colorado river basin.
878 *Water*, **14 (23)**, 3813.

879 Tinkham, W. T., A. M. S. Smith, H.-P. Marshall, T. E. Link, M. J. Falkowski, and A. H. Winstral,
880 2014: Quantifying spatial distribution of snow depth errors from LiDAR using random forest.
881 *Remote Sens. Environ.*, **141**, 105–115.

882 Tsang, L., and Coauthors, 2022: Review article: Global monitoring of snow water equivalent using
883 high-frequency radar remote sensing. *The Cryosphere*, **16 (9)**, 3531–3573.

884 Versegny, D. L., 2007: Class-A canadian land surface scheme for GCMS. i. soil model. *Int. J.*
885 *Climatol.*, **11 (2)**, 111–133.

886 Vögeli, C., M. Lehning, N. Wever, and M. Bavay, 2016: Scaling precipitation input to spatially
887 distributed hydrological models by measured snow distribution. *Front Earth Sci. Chin.*, **4**.

888 Williams, A. P., B. I. Cook, and J. E. Smerdon, 2022: Rapid intensification of the emerging
889 southwestern north american megadrought in 2020–2021. *Nat. Clim. Chang.*, **12 (3)**, 232–234.

890 Winstral, A., D. Marks, and R. Gurney, 2014: Assessing the sensitivities of a distributed snow
891 model to forcing data resolution. *J. Hydrometeorol.*, **15 (4)**, 1366–1383.

892 Wrzesien, M. L., and Coauthors, 2022: Development of a “nature run” for observing system
893 simulation experiments (OSSEs) for snow mission development. *J. Hydrometeorol.*, **23 (3)**,
894 351–375.

895 Xu, Z., E. R. Siirila-Woodburn, A. M. Rhoades, and D. Feldman, 2022: Sensitivities of subgrid-
896 scale physics schemes, meteorological forcing, and topographic radiation in atmosphere-
897 through-bedrock integrated process models: A case study in the upper colorado river basin.
898 *EGUsphere*, 1–29.